J. Fluid Mech. (2007), *vol.* 583, *pp.* 313–345.
doi:10.1017/S0022112007006337 Printed in the United Kingdom

Fire whirls due to surrounding flame sources and the influence of the rotation speed on the flame height

RUI ZHOU[1] AND ZI-NIU WU[1]†

[1]Department of Engineering Mechanics, Tsinghua University, Beijing 100084, China

(Received 30 June 2006 and in revised form 10 February 2007)

In this paper, we use numerical simulation and laboratory experimental observation to show that fire whirls can be generated spontaneously through the interaction between a central flame and surrounding organized or randomly distributed flames. The momentum of the air stream entrained by the main flame decreases as it crosses a surrounding flame, so that the main flame rotates if surrounding flames are arranged in such a way as to block the passage of the air stream directed towards the centre of the main flame and to favour flows in a particular circumferential direction. An analysis is performed to study the role of the rotation speed in the flame height. It is found that the flame height initially decreases to a minimum owing to the inflow boundary layer wind reducing the initial vertical velocity of gas for low rotation speed and to entrainment enhancement reducing the rising time, and then it increases owing to the pressure reduction at the centre of the rotating vortex and entrainment suppression extending the rising time.

1. Introduction

The interest in studying fire whirls comes not only from their beauty as a natural phenomenon but also from their disastrous effects (Graham (1952, 1957)). Fire whirls are highly destructive since intense rising due to spiralling spreads burning scraps far away to generate new fire sources. Fire whirls are also important because the resulting circulation enhances consumption of the fuel producing a greater source of smoke and toxic products. The swirling in a fire whirl was initially thought to be induced by an external source of angular momentum (Emmons & Ying 1967; Satoh & Yang 1996), by atmospheric instability or by the interplay of wind and topography (Graham 1957). The characteristics of fire whirls have been studied experimentally and numerically through plume flows in a rotating cylinder or by strategically arranged surrounding solid walls (Emmons & Ying 1967; Satoh & Yang 1996; Battaglia *et al.* 2000*a*; Farouk, McGrattan & Rehm 2000), or analytically through imposition of an inviscid vortex assumption (Battaglia, Rehm & Baum 2000*b*). Emmons & Ying (1967) conducted one of the earliest studies to investigate the fire whirl phenomena experimentally. A fire whirl was formed from a liquid-fuel pool at the centre of a rotating cylindrical screen which imparted a controlled angular momentum to the ambient air. Later Satoh & Yang (1996) conducted experiments on a flame surrounded by a four-walled square enclosure with symmetric corner gaps between

† Author to whom correspondence should be addressed: ziniuwu@tsinghua.edu.cn

the walls, and open at the top. As the fire burns in the centre, ambient air is continuously entrained through the gaps into the plume to produce swirling. These two representative experimental studies have been simulated numerically by Battaglia *et al.* (2000*a*), Farouk *et al.* (2000) and Meroney (2003*a*, *b*, 2004) using computational fluid dynamics. It is commonly accepted that the formation of fire whirls requires a source of ambient vorticity, a concentrating mechanism, and a favourable environment for their stability and growth (Meroney 2003*a*). The concentrating mechanism rotates the horizontal vorticity into the vertical direction and stretches the vortex tubes.

Experimental and numerical studies on a plume contained in a rotating cylinder (Emmons & Ying 1967; Battaglia *et al.* 2000*a*) have shown that the flame height varies due to the swirl motion. Emmons & Ying (1967) observed by experiment that the plume is lengthened with whirl. The numerical results of Battaglia *et al.* (2000*a*) indicate that the flame height first decreases with whirl to a minimum before increasing as the whirl increases further. Chigier *et al.* (1970) performed experiments that demonstrated that plume height grows with increased rotation, but then over-rotation suppressed it.

The above studies reveal the structure (such as temperature distribution and length) of fire whirls, showing that swirling of a flame lengthens the fire column vertically and tightens it radially, conducive to the more rapid spread of fire sources and to the increase of the time-averaged burning rate. To the best of the authors' knowledge, most previous studies of mechanisms and characteristics of fire whirls are based on externally modifying the geometry surrounding fire plumes, such as imposing a rotating cylinder or an external circulation. No attempt has been made to investigate whether fire whirls can occur spontaneously in nature, without the existence of an imposed external circulation. No theory has been developed to describe the relationship between the rotation speed and the flame height. However, there is work on the influence of the rotation speed on the propagation of fluid along a vortex tube. For instance, Atobiloye & Britter (1994) carried out a simplified analysis of the influence of vortical structures on a two-density fluid that indicates possible motion of the light fluid into the heavy one and vice versa. The fluid velocities along the vortex tube were found to vary as the angular speed (for a solid-body rotation) or the vortex strength (for a free vortex) changes.

The purpose of the present study is to show, with the use of numerical computation and experiment, that fire whirls can be generated spontaneously through the interaction between a main flame and organized or randomly distributed surrounding flames. This is inspired by the work of Satoh & Yang (1996) who built four solid walls with gaps to surround the centre flame. Here the solid walls are replaced by three or more regularly or randomly distributed flames. Furthermore, we analyse the influence of the rotation speed on the height of the flame.

In § 2, we will first describe a basic four-flame-wall configuration for which we find rotation through numerical simulation and laboratory experiments. Then, we use numerical simulation to study more configurations, including regularly distributed three-wall and six-wall models, and randomly distributed surrounding walls. We will demonstrate that rotation of the main flame can also be induced by randomly distributed flame sources. A criterion based on the definition of gap fraction will be given for establishing the likelihood of a fire whirl for a given fire geometry. The numerical tools used in this section are briefly outlined in Appendix A.

In § 3, we will study the influence of the rotation speed on the height of the rotating flame. We will show that the flame height is related to the buoyancy force, which itself is an increasing function of the rotation speed, to the initial vertical velocity of the

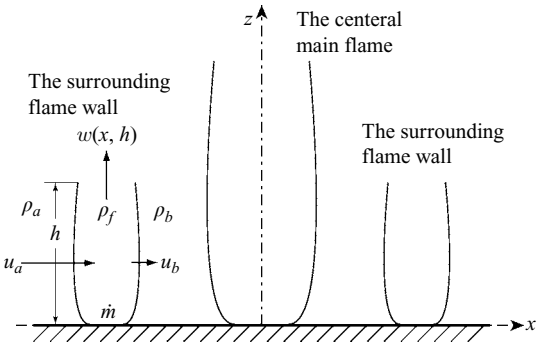

FIGURE 1. A planar two-dimensional flame configuration.

flame and to the rising time. The initial vertical velocity, defined as the axial velocity at the top of the boundary layer, is shown to be a decreasing function of the rotation speed. And the rising time, defined as the time it takes for fuel gas to be mixed with entrained air at the stoichiometric ratio, is shown to be a function of the rotation speed, which decreases then increases. With these conclusions we will prove that the flame height first decreases to a minimum and then increases when the rotation speed increases.

The essential findings of this paper are summarized in § 4, where we also outline some subjects that deserve further study.

2. Fire whirls due to surrounding flame sources

In this section we aim to demonstrate that surrounding flame walls can induce rotation of the main flame if the surrounding flames are placed asymmetrically. After arguing that the horizontal momentum of an air stream weakens while crossing a flame wall, we give a four-flame-wall model for which we display rotation from both numerical and experimental observations (§§ 2.1 and 2.2). We also give more realistic configurations, including regularly distributed three-flame-and six-flame-wall models and randomly distributed flame walls (§ 2.3). Then we study the role of the free passag of air stream in the rotation speed (§ 2.4) to give some indication of how flame distributions quantitatively influence rotation. Finally, we briefly discuss the possibility of flame distribution that induces rotation (§ 2.5).

2.1. *Fire whirl produced by a four-flame-wall model*

Qualitatively, it is not difficult to understand why a surrounding flame weakens the momentum of the air stream entrained by a main flame. Consider for instance a planar two-dimensional flame configuration as displayed in figure 1, composed of a main flame surrounded by two flame walls. We use ρ and T to denote the density and the temperature, respectively. The subscripts a, b, and f refer to conditions in the atmosphere, between the main flame and the surrounding flame, and inside the main flame, respectively. The buoyancy force inside the surrounding flames induces an upward motion; that is, inside the surrounding flames, the vertical component w of the velocity satisfies $w > 0$. Consider the left-hand surrounding flame of height h. By mass conservation we have

$$\dot{m} + \int_0^h \rho_a u_a \, \mathrm{d}z = \int_0^h \rho_b u_b \, \mathrm{d}z + \int_{sur} \rho_f w(x, h) \, \mathrm{d}x \tag{2.1}$$

Fuel	Molecular formula	The chemical equation	The stoichiometric ratio
acetone	CH_3COCH_3	$CH_3COCH_3 + 4O_2(20air) = 3H_2 + 3CO_2$	$58 : 580 = 0.100 : 1$
alcohol	C_2H_5OH	$C_2H_5OH + 3O_2(15air) = 3H_2 + 2CO_2$	$46 : 435 = 0.106 : 1$
carbon	C	$C + O_2(5air) = CO_2$	$12 : 145 = 0.093 : 1$

TABLE 1. The stoichiometric ratio of acetone, alcohol and carbon to air, 20air, 15air and 5air denote the equivalent quantity of air containing the required O_2.

where the left-hand term $\dot{m}$ represents the mass added by the combustion source and the right-hand term $\int_{sur} \rho_f w(x, h)\,\mathrm{d}x$ represents the mass flow across the top of the left-hand surrounding flame. Generally, the mass of fuel is small compared to that of the air. Considering the case of complete reaction, we use the chemical equation to calculate the stoichiometric ratio of three kinds of common fuels to air, as listed in table 1. Here acetone is the fuel used by Emmons & Ying (1967) in their experiments, alcohol is the fuel used in our experiments and carbon is the main component of wood or other combustible materials. It is easy to see that the mass of fuel is about one order smaller that of the air. It may be even smaller in an open fire. Therefore, the mass added by the combustion source $\dot{m}$ in equation (2.1) can be neglected. Since $\int_{sur} \rho_f w(x, h)\,\mathrm{d}x > 0$, we have

$$\int_0^h \rho_b u_b\,\mathrm{d}z < \int_0^h \rho_a u_a\,\mathrm{d}z.$$

This means that the total momentum decreases while the air stream travels from a surrounding flame.

Therefore, unconnected surrounding flame walls could induce rotation of the main flame if they were placed in such a way as to partially block the air stream directed towards the centre of the main flame and to favour flows in a particular circumferential direction of the main flame. Figure 2(*a*) displays such a configuration. It is composed of a main pool (pool *D*), placed at the centre, and four side pools. As shown in figure 2(*b*), a strong plume rises above the centre of pool *D*. Four side pools each produce a flame wall. Owing to the buoyancy inside the main plume, there is a radial movement of the surrounding air towards the centre of the plume. Part of this radially moving air moves freely through open sections like *A*, while part will travel across flame walls like section *B*. Since the horizontal air stream crossing a flame wall loses part of its horizontal momentum due to the rising motion in the flame wall, the radial inward flow momentum is strong in section *A* and weak across section *B*. This produces a net angular momentum which should rotate the main flame.

In order to show that the centre flame rotates, we have performed a numerical computation for the four-flame-wall model. Details of the numerical method are given in Appendix A and its reliability is checked by comparison to published data, details of which are given in an Appendix available with the online version of the paper. Figure 2(*c*) displays time-averaged streamlines of the flow based on the numerical computation, showing a counterclockwise rotation of the centre plume. The isosurface of the 5 % mixture fraction is used to represent the plume. Theoretically the plume is the surface on which the mixture fraction of fuel is zero as the fuel is completely oxygenated by the air. However, it is impossible that the mixture fraction precisely equals zero and a small value can be used instead, the isosurface of which denotes

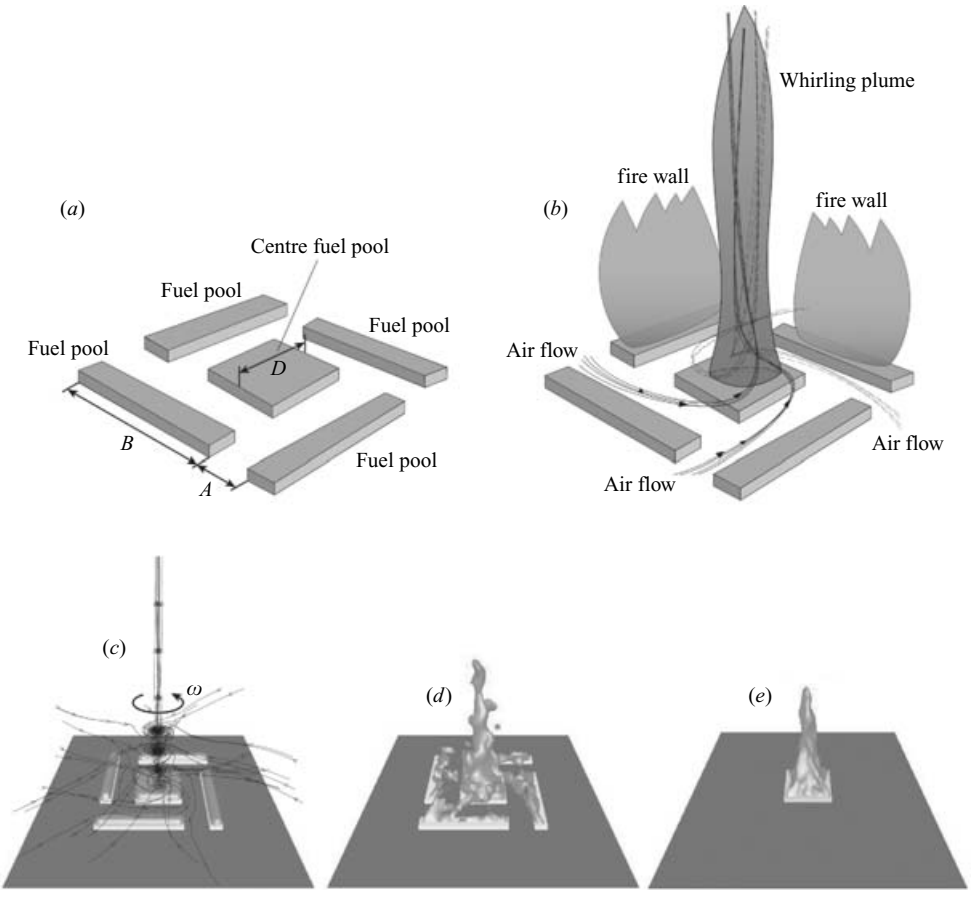

FIGURE 2. Basic auto-rotating fire whirl model. (*a*) Fuel pool layout. (*b*) Main trajectories of the surrounding air entrained by the centre plume. (*c*) Time-averaged streamlines based on numerical results, showing a counterclockwise rotation of the centre plume. (*d*) Fire whirl produced by numerical simulation, with $A/D = 0.5$ and $D = 2m$. (*e*) Flame without a surrounding flame wall.

the interface between fuel-rich and fuel-lean regions of the fire, roughly representing the plume. The precise value is not very important. In the present work, 5 % is used as it gives a good view. The computed plumes are displayed in figure 2(*d*). The rotation of the centre plume is obvious from the helical shape of the isosurface. The time-averaged rotation speed of the main flame at height $z/D = 0.5$ is $13.2\,\mathrm{s}^{-1}$.

To show that the rotation is indeed induced by the asymmetry of the surrounding flame walls, we have done another computation with the flame walls removed. In this case, no rotation occurs, as can be seen from figure 2(*e*).

It is interesting to compare the height of the main flame with and without rotation. The flame height is roughly defined as the top of the 5 % isosurface. The height of the rotating plume is 6.5 m while the non-rotating plume is 5.2 m. Hence rotation increases the height of the flame. The role of rotation in the flame height will be further studied in § 3. Since the flow is turbulent, the flame heights are time dependent and unsteady. An experimental fire whirl driven by a rotating cylinder (Emmons & Ying 1967; Satoh & Yang 1996; Emmons & Ying 1967) initially precesses slowly with a low height before finally rising to its full height. In our fire-wall models there

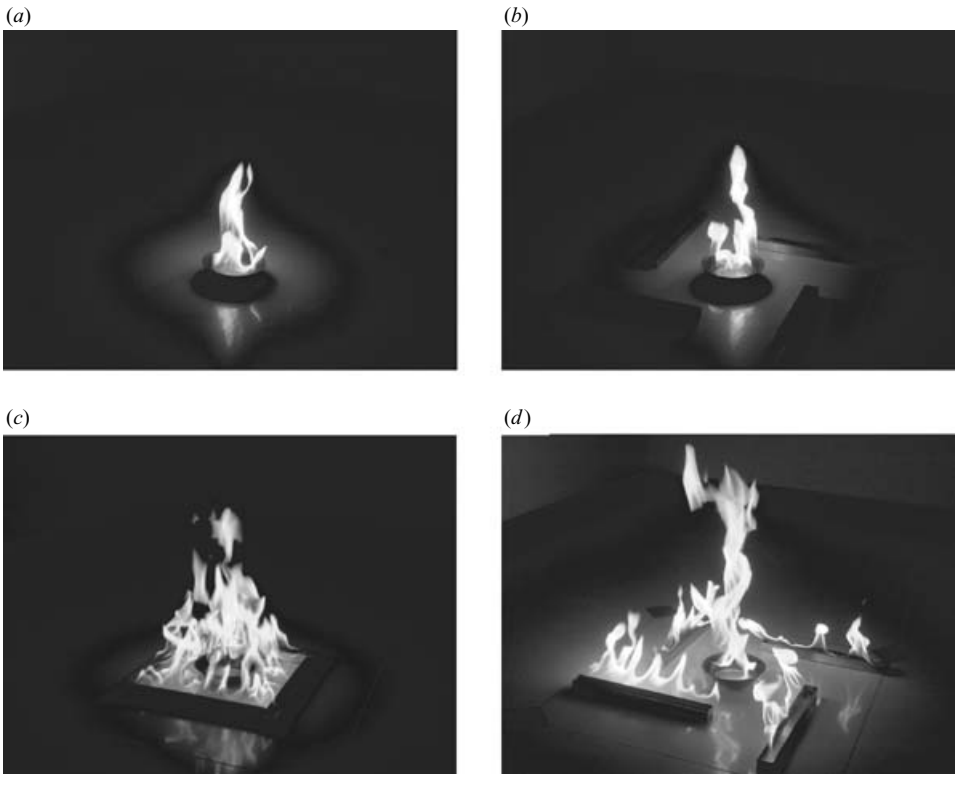

FIGURE 3. Photographs of laboratory-produced flames with and without rotation. (*a*) An unconfined plume. (*b*) A plume in the centre of unburned fuel polls. (*c*) A plume in the centre of closed flame walls. (*d*) A plume in the centre of four flame walls with gaps between.

is intermittency for low- and high-speed rotation. We measure the height when the rotation is the highest for a given configuration.

2.2. *Experimental observation*

In order to verify the above results, we have performed experiments for the four-flame-wall configuration. In the experiment, the centre fuel pool is a round container with diameter of 13 cm and height of about 5 cm. Side fuel pools are rectangular containers with dimensions of $30\,\mathrm{cm} \times 3\,\mathrm{cm} \times 2\,\mathrm{cm}$. Though the container height might have some influence on the flame physics and flame height, it does not affect the qualitative properties we are interested here. All the containers were made of stainless steel, filled with alcohol, whose heat of combustion is $3.02 \times 10^7\,\mathrm{J\,kg^{-1}}$. The side pools were organized in a similar way as in figure 2(*a*). The gap width is 15 cm so that $A/D \approx 1.0$. In order to avoid any undesirable disturbances and to provide enough space for the ambient atmosphere, the experiment is performed in a closed empty room, which is about 3 m high and with solid walls more than 1 m from the flame pools. The ambient (room) temperature is 16 °C.

All the images were captured by a digital camera BenQ S40, with a total resolution of 2304×1728 pixels, and cropped to the required size. The photographs for the four-flame-wall model are displayed in figure 3. First we display three cases for which the centre flame does not rotate:

(i) the centre pool (flame) has no surrounding pools (flame walls), as displayed in figure 3(*a*);

(ii) the side pools do not burn, as seen in figure 3(*b*);

(iii) there is no gap between the side pools, i.e. the side flames form a closed set, as shown in figure 3(*c*). It appears that the flame height for the fully blocked case (iii) is slightly higher than in the unblocked case. This is due not to rotation but to the unsteadiness of the flame. Occasionally a portion of the flame tears off from the main flame to rise to a higher altitude.

The centre flame rotates when these are four flame walls with gaps between them, as demonstrated in figure 3(*d*).

In the experiment, we also found that rotation increases the height of the flame. The flame without rotation has a height of 30 cm, while the rotating flame reaches a height of 60 cm.

Hence, experimental observation confirms the numerical conclusions that autorotation occurs when surrounding flames partially block the inward air flow and favour the passage of the air stream through the gaps, provided that this air stream is aligned approximately in the direction of rotation. Moreover, the flame height increases due to rotation.

2.3. *Fire whirls produced by multiple or randomly distributed surrounding flames*

Here we consider more configurations for which the centre flame rotates. Figure 4 displays a three-flame-wall model and a six-flame-wall model. The numerical details for the computation of these two configurations are given in Appendix A.

For the three-flame-wall model, the centre pool is a triangle. Each side flame is parallel to one side of the triangle. The air stream through the gaps (A) lies in a particular circumferential direction with respect to the centre pool. In figure 4(*a*) we display some representative time-averaged streamlines and the 5 % isosurface representing the flame. It is clear that the centre flame has an anticlockwise rotation.

For the six-flame-wall model, the centre pool is a hexagon. Each of the six side flames is parallel to one side of the hexagon. The gaps are constructed such that the air stream through the gaps (like A) again lies in a particular circumferential direction with respect to the centre pool. In figure 4(*b*) we show time-averaged streamlines and flame shapes. The centre flame rotates. The computation yields different rotation speeds for the three-, four- and six-flame-wall models. In figure 4(*c*) we display the time-averaged circumferential velocity at height $z = 1$ m. We see that the greater the numbers of flame walls, the faster the flame rotates.

In reality, the likelihood of naturally having regularly distributed flame sources as shown in figures 2 and 4 is quite small. Flame sources are more frequently randomly distributed in a real fire disaster. Extrapolating from the autorotation mechanism observed for the above models, it is possible to construct an infinite number of flame source distributions capable of sustaining/enhancing or avoiding/weakening fire whirls. Now we consider randomly distributed flame sources surrounding a main flame. We just display some configurations for which the surrounding flame sources favour flows of the main flame in a particular circumferential direction and induce rotation.

In figure 5 we display a random flame source distribution. The time-averaged streamlines displayed in figure 5(*a*) show a strong rotation. The flames in figure 5(*b*) show that the rotating centre flame is higher than the surrounding flame. The strong autorotation of the central flame is mainly due to the large gaps at the upper right

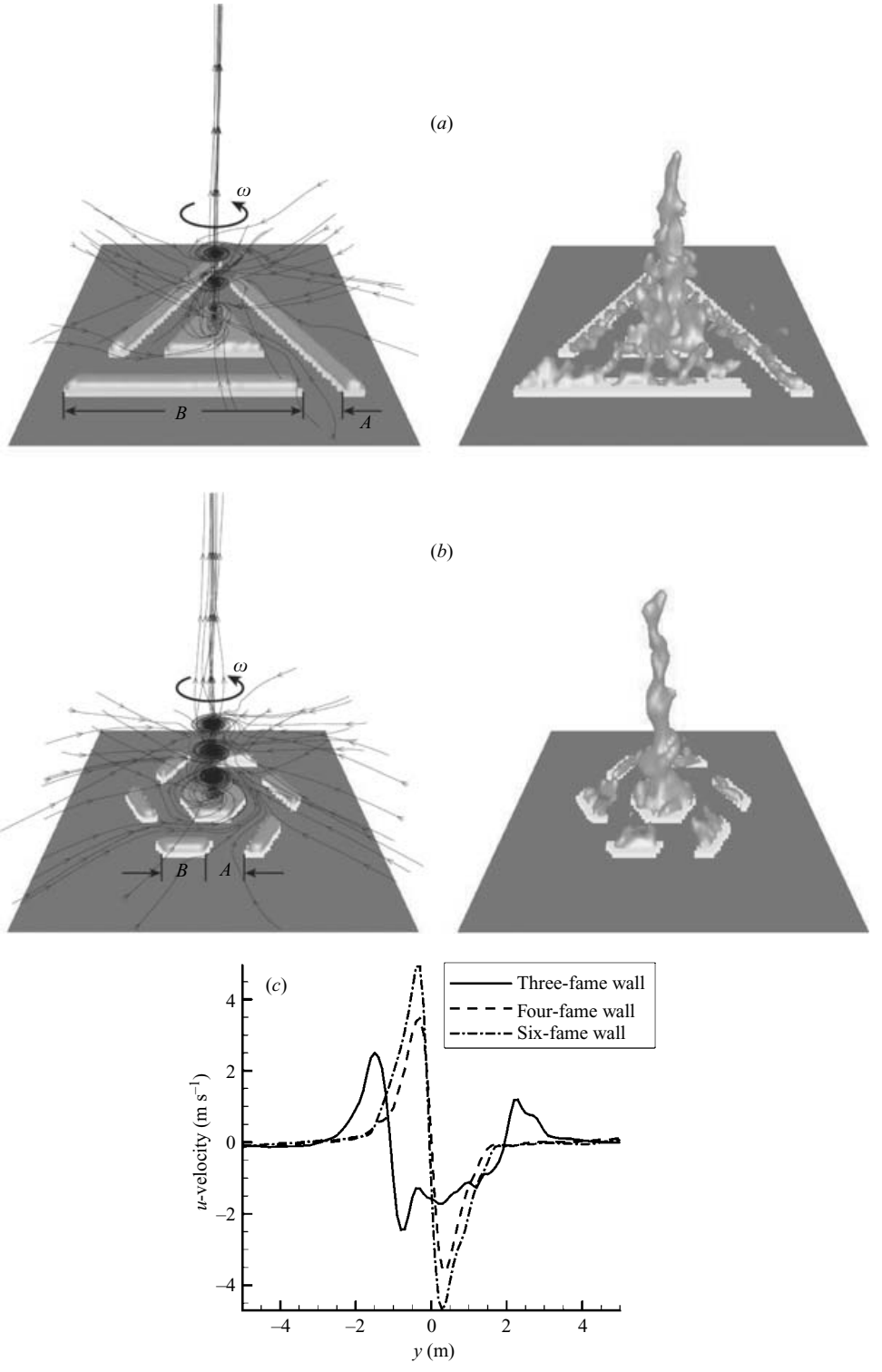

FIGURE 4. Two further configurations with autorotation. (*a*) Three-flame-wall model showing streamlines and the computed flame. (*b*) Six-flame-wall model. (*c*) Time-averaged swirl velocity profiles at $z = 1$ m for the different models.

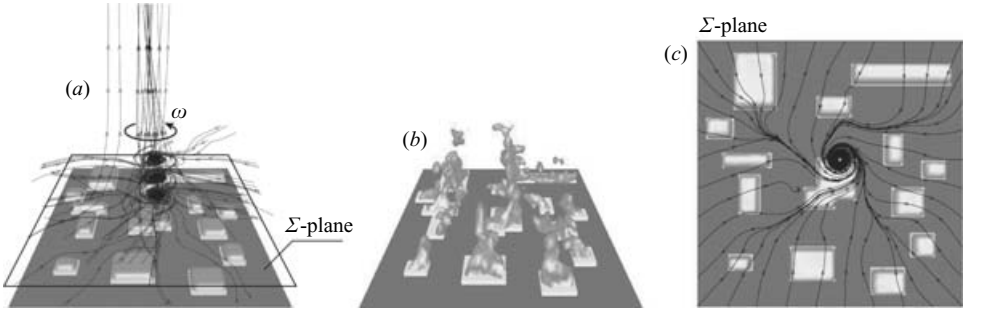

FIGURE 5. Computed results for randomly distributed flame sources. (*a*) Time-averaged streamlines showing an intense rotating and upward motion. (*b*) View of burning plumes. (*c*) Time-averaged streamlines on a horizontal plane.

corner and upper left corner of the layout (figure 5*c*). The air stream entering through these corners lies in a particular circumferential and anticlockwise direction with respect to the main flame.

To see this more clearly, we constructed other configurations. In figure 6(*a*), we display an isolated flame. Without the influence of surrounding flames, it does not rotate, as seen from the time-averaged streamlines directed to the centre of the flame. In figure 6(*b*), we show a two-main-flame configuration. For the left main flame, the lower left and upper left gaps between the surrounding flames lie in a direction such as to generate an anticlockwise rotation. The time-averaged streamlines obtained by numerical computation show such a rotation. For the right main flame, the situation is reversed, and we obtain a clockwise rotation numerically. In figures 6(*c*) and 6(*d*), we display two different configurations, with the gaps chosen to favour rotation in opposite directions. In figure 6(*c*), the dominant air passage (gap) through the arbitrarily distributed flame sources is obviously in the circumferential and clockwise direction about the main flame, thus generating a clockwise rotation. In figure 6(*d*), the dominant air passage is obviously in the circumferential and anticlockwise direction about the main flame, thus generating an anticlockwise rotation.

2.4. *On the role of gap fraction*

As we have argued, the rotation is due to the coexistence of flame walls and gaps: the former partially block the air stream, while the latter favour flows in a particular circumferential direction. It would be interesting to see how the gap width influences autorotation; it depends on many factors such as the number of side flames, shape of the flames, distance between the centre flame and the side flames, thickness of the side flames, etc. Detailed numerical computations can only yield quantitative results for specific conditions. Here we consider the rotation speed as a function of gap fraction defined as

$$\eta_n = A/(A + B)$$

for regularly distributed flame walls, where A is the gap length as shown in figures 2 and 4, B is the length of each flame wall. If the width C of the surrounding flame walls is not negligible, we may use $\eta_n = A/(A + B - C)$ to define the gap fraction. In table 2, we give the gap fractions, rotation speeds and flame heights for the three-wall, four-wall and six-wall-models computed previously. The six-flame-wall model has the largest gap fraction and the rotation speed is the highest.

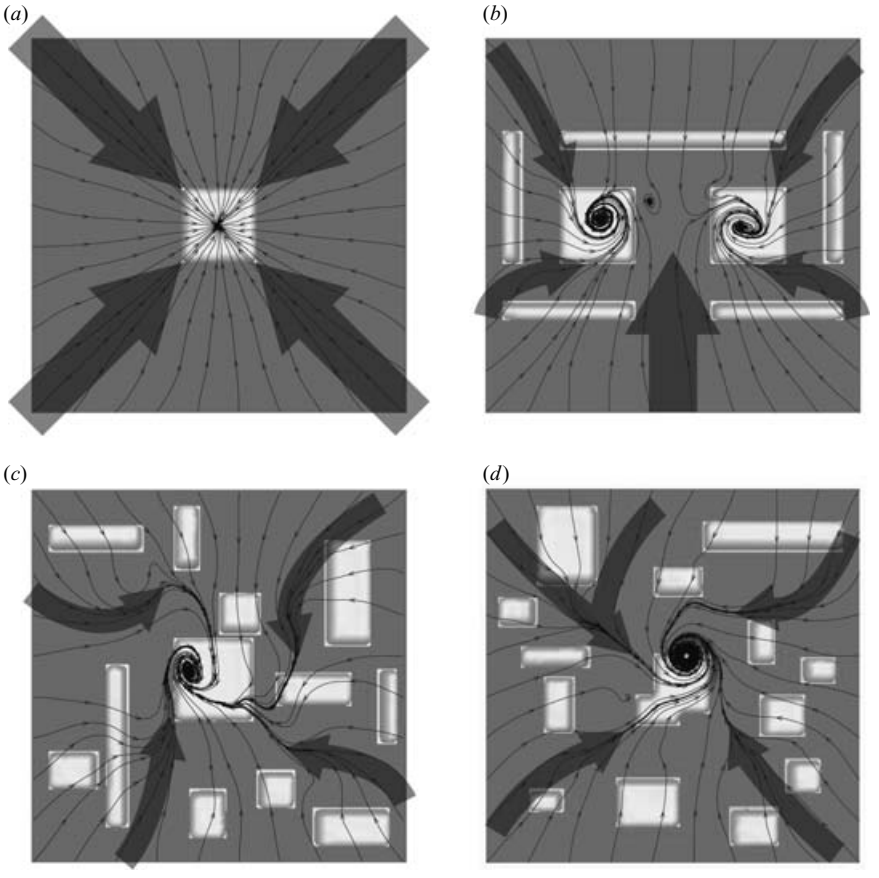

FIGURE 6. Computed results showing the passage of air streams for different configurations. (*a*) For a single plume air moves toward it directly without rotation. (*b*) A configuration of organized flame sources generating a pair of fire whirls. (*c*) A configuration of randomly distributed flame sources generating a clockwise fire whirl. (*d*) A configuration of randomly distributed flame sources generating an anticlockwise fire whirl.

n	η_n	$\omega\,(\mathrm{s}^{-1})$	$H\,(\mathrm{m})$
3	0.143	12.0	6.3
4	0.250	17.5	6.5
6	0.575	25.0	7.2

TABLE 2. The influence of the number of flame walls (n) (with different gap fraction η_n) on the angular velocity (ω) and the flame height (H).

When there are no flame walls, $\eta_n = 1$, and when the flame walls form a closed set, $\eta_n = 0$. The flame does not rotate in these two cases; hence the rotation speed must increase to a maximum and then decrease when the gap fraction increases. The gap fraction $\eta_{n,opt}$ produces the highest autorotation. It can be conjectured that $\eta_{n,opt} \approx 1/2$, and this can be explained by considering a layout with anticlockwise rotation such as in figures 2 and 4. For $\eta_n < 1/2$ the continuous increase of η_n means

η	0.000	0.125	0.250	0.375	0.500	0.625	0.750	0.875	1.000
$\omega\,(\mathrm{s}^{-1})$	0	5.539	17.447	32.386	35.172	19.381	16.646	2.714	0

TABLE 3. The influence of the gap fraction (η) on the angular velocity (ω) for four-flame-wall fire whirls.

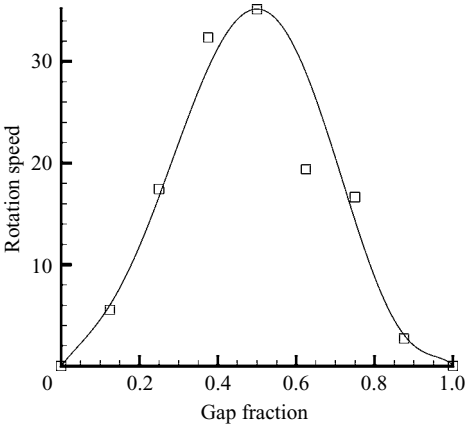

FIGURE 7. Dependence of the rotation speed on the gap fraction: squares, data; curve, fitted polynomial.

more angular momentum added to the main flame to favour anticlockwise rotation, whereas when $\eta_n > 1/2$ part of the air stream through the gaps will contribute a negative angular momentum so that rotation decreases. In order to check this, we consider the four-wall model with differen gap fractions. Table 3 gives the data obtained by numerical computation. In figure 7 we display a polynomial fit of the relation $\omega = \omega(\eta_n)$ by using the data of table 3; we find that $\eta_{n,opt} \approx 1/2$.

For other regularly distributed flame wall models, we have similar results. Hence we have the following criterion for whether or not a fire whirl occurs:

Criterion. For a flame surrounded by regularly distributed flame walls, rotation occurs if the gap fraction lies between 0 and 1, and maximum rotation occurs when the gap fraction is 1/2.

For the case of non-regular or randomly distributed flame sources, it is not convenient to relate the rotation speed to the gap fraction and to define a criterion for fire whirl, since there is some uncertainty in defining this fraction. In figure 8, we provide some examples for which the gap fraction is above 0 but the central flame does not rotate.

In figure 8(*a*), the gap fraction is close to 1 and there is no rotation. In figure 8(*b*), the gap fraction lies within 0 and 1 but each gap generates an independent vortex. This shows that for the central flame to rotate these must be a sufficient number of gaps (at least 3). If two flame walls form a corner, then the vortex is captured by the corner and does not add angular momentum to the central flame. In figure 8(*c*), the gap fraction still lies between 0 and 1 and close togethers two gaps generate a unique vortex that is not at the centre of the main flame. In figure 8(*d*), there are two gaps: one generates a stream in the clockwise direction and the other in the anticlockwise

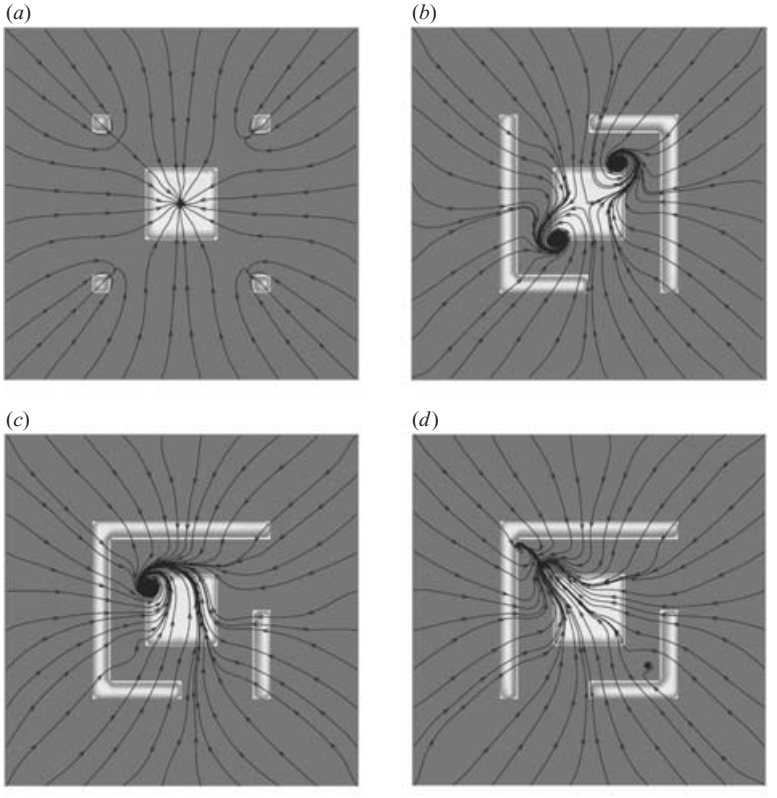

FIGURE 8. Several particular situations for which there is no rotation or the rotation is not around the central flame.

direction so that there is no rotation. Thus, we are unable to give general criteria for randomly distributed flame sources.

2.5. *Regularly or randomly distributed flame sources*

In a real fire disaster, interaction between wind and flame sources, non-uniformity of combustion and the existence of topography may yield source configurations similar to or different from those presented above. Nonetheless, if there are gaps oriented to favour the passage of an air stream in such a direction as to augment the angular momentum of a main flame, the flame rotates. The coexistence of particular geometry topography, wind, and surrounding fires may also induce fire whirls.

Next we provide an example of fire whirl that might have been induced by a combination of geometry and surrounding fires.† A fire occurred in Manitoba, Canada, in the flax storage compound of Eucata Fibers on 19 April 2000. Bales were arranged in a rectangular array. There were 1000 bales per stack in 42 stacks packed 30 feet high. The stacks were separated by 200 feet and spread over 160 acres (2640×2640 ft; or 800×800 m) Each stack was approximately 250 ft wide $\times$ 250 ft long $\times$ 30 feet high ($75\,\text{m} \times 75\,\text{m} \times 10\,\text{m}$). This is very similar to an urban area with three-storey apartment complexes. Lightning hit the stacked bales, a fire started, and

† This example was kindly provided by a referee of this paper.

fire whirls were reported in the centre region. A pickup truck driving by was lifted from the ground and flipped over.

Multiple flame sources also exist for large-scale city fires. Satoh *et al.* (2005) experimentally studied interaction among multiple fires in equidistant fire arrays. They found that the vigorous burning in the array central region tends to cause the fires there to merge and the merging flames grow into the gigantic fire whirl if wind is blowing into one corner of the array. This can be considered as an example of fire whirl induced by interaction between multiple fires and wind.

3. Height of the rotating flame

As noted in the Introduction, there are some experimental and numerical studies on a plume contained in a rotating cylinder, which have shown that the flame height varies due to the swirl motion. In § 2, we also observed that the height of the flame depends on the rotation speed (see table 2). Here we consider an axisymmetrical flame subjected to a given rotation speed and study the dependence of the flame height on the rotation speed.

A real fire whirl involves many complex phenomena. The present analysis is based on the following assumptions or simplifications: (i) The combustion is mixing-controlled and the reaction of fuel and oxygen is infinitely fast. This assumption is also used in our computation by the fire dynamics simulator (FDS), as the mixture fraction combustion model. (ii) It takes a time τ (defined as the rising time) for fuel gas to be mixed with entrained air at the stoichiometric ratio. A fuel particle goes upwards during the rising time τ and reaches a final height of H, which is defined as the flame height. (iii) When evaluating the buoyancy force an averaged value T_f of the temperature inside the flame is used. (iv) When evaluating the buoyancy force, viscous dissipation is not considered. (V) For the boundary layer on the floor, a viscous thin-layer model is considered. (vi) The radius of the flame is much smaller than its height, but since at the base of the flame we have used a viscous thin-layer model (assumption (v)), we do not need this assumption. (Vii) As explained in § 2.1, the mass added by the combustion source is so small that it can be neglected.

With these approximations, we will be able to capture the main physics and obtain a very simple expression describing the relationship between the rotation speed and flame height. As shown in figure 9, the height of the rotating flame depends not only on the rotation speed ω (which reduces the pressure thus increasing the buoyancy force inside the flame) but also on the initial vertical velocity V_{z0} at the top of the boundary layer. The initial vertical velocity V_{z0} is itself a function of the rotation speed. The rising time τ varies with the rotation speed as well.

The analysis is split into four main steps:

1st step. In this step, as detailed in § 3.1, we study the role of rotation in increasing the buoyancy force for the part of the flame above the boundary layer. The rotation is shown to decrease the pressure, and thus increase the buoyancy force inside the flame. Along the centreline of the plume, the buoyancy force acts to accelerate the rising motion, which can be expressed as

$$f_z \sim \overline{f}_z + A_2\omega^2, \tag{3.1}$$

where

$$\overline{f}_z = \beta(T_f - T_0)g$$

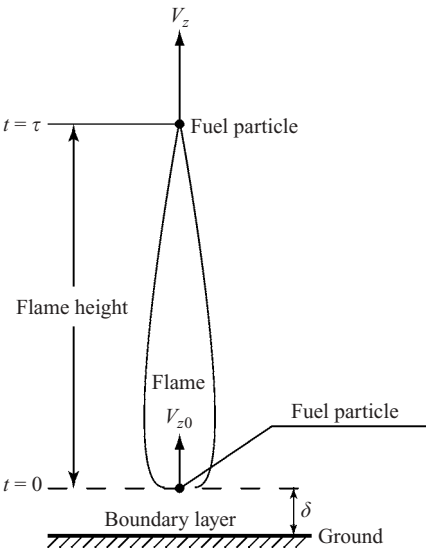

FIGURE 9. A simple model of the flame.

is the buoyancy force in the case without rotation, and

$$A_2 = \frac{r_0^2}{2RT_f}[1 + \beta(T_f - T_0)]g$$

is a derived parameter, where β is the volume expansion coefficient of the gas, T_0 is the temperature of the ambient gas, T_f is the temperature of the flame, r_0 is the averaged radius of the flame, R is the gas constant, and g is the gravitational acceleration. According to the definitions of τ and H, the flame height is given by

$$H = \tfrac{1}{2} f_z \tau^2 + V_{z0}\tau, \tag{3.2}$$

where both V_{z0} and τ are ω-dependent, to be solved in following steps.

2nd step. This step, as detailed in § 3.2, is concerned with the perturbation of initial vertical velocity due to rotation. We shall prove that this perturbation satisfies relation

$$V'_{z0} \sim -k_1 r_0 \omega,$$

so that

$$V_{z0} \sim \overline{V}_{z0} - k_1 r_0 \omega, \tag{3.3}$$

where $\overline{V}_{z0}$ is the initial vertical velocity in the case without rotation and k_1 is a non-dimensional parameter independent of ω. Hence, the rotation decreases the initial vertical velocity.

3rd step. This step, as detailed in § 3.3, concerns the influence of rotation on the rising time. We have shown that the rotation first enhances the entrainment then suppresses it (see Appendix E), thereby first slowing the rate of air/fuel mixing then speeding it up. The expression for the rising time is

$$\tau \sim \overline{\tau} - D_1\omega + D_2\omega^2, \tag{3.4}$$

where

$$\overline{\tau} = (E - 1)\frac{\overline{V}_{z0}}{\beta(T_f - T_0)g}$$

is the rising time in the case without rotation, and

$$D_1 = (E-1)\frac{k_1 r_0}{\beta(T_f - T_0)g},$$

$$D_2 = \frac{r_0^2 \overline{V}_{z0}}{2RT_f}\left\{\frac{m\rho_{fuel} r_0^2 \beta(T_f - T_0)}{4\rho_0}\frac{\displaystyle\int_0^{r_0}\left(1-\frac{r^2}{r_0^2}\right)B(r)r\,\mathrm{d}r}{\displaystyle\left[\int_0^{r_0} B(r)r\,\mathrm{d}r\right]^2}E - E + 1\right\} \times \frac{1+\beta(T_f - T_0)}{\beta^2(T_f - T_0)^2 g},$$

$$E = \exp\left\{\frac{m\rho_{fuel} r_0^2[1+\beta(T_f - T_0)]}{4\rho_0 \displaystyle\int_0^{r_0} B(r)r\,\mathrm{d}r}\right\}$$

are derived parameters, where ρ_{fuel} is the averaged density of fuel gas inside the flame, ρ_0 is the background density, m is the stoichiometric ratio of air to fuel, and $B(r)$ is an unknown non-dimensional function of r.

4th step. In this step, as detailed below, we will use the results obtained in the previous three steps and some further analysis to show that the height of the flame can be described by $H \sim H_0 + L(\omega - \omega_0)^2$.

Inserting (3.1), (3.3) and (3.4) into (3.2), we obtain the following expression for the flame height:

$$H \sim \tfrac{1}{2}(\overline{f}_z + A_2\omega^2)(\overline{\tau} - D_1\omega + D_2\omega^2)^2 + (\overline{V}_{z0} - k_1 r_0\omega)(\overline{\tau} - D_1\omega + D_2\omega^2),$$

or

$$H \sim \overline{H} - L_1\omega + L_2\omega^2 - L_3\omega^3 + L_4\omega^4 - L_5\omega^5 + L_6\omega^6, \tag{3.5}$$

where

$$\overline{H} \sim \tfrac{1}{2}\overline{f}_z\overline{\tau}^2 + \overline{V}_{z0}\overline{\tau}$$

is the flame height in the case without rotation, and the series of terms of ω represent the influence of rotation on the flame height, with coefficients

$$\left.\begin{aligned} &L_1 = \overline{f}_z D_1\overline{\tau} + D_1\overline{V}_{z0} + k_1 r_0\overline{\tau},\\ &L_2 = \tfrac{1}{2}\overline{f}_z D_1^2 + A_2\overline{\tau}^2 + \overline{f}_z D_2\overline{\tau} + D_1 k_1 r_0 + D_2\overline{V}_{z0},\\ &L_3 = A_2 D_1\overline{\tau} + \overline{f}_z D_1 D_2 + D_2 k_1 r_0, \quad L_4 = \tfrac{1}{2}A_2 D_1^2 + \tfrac{1}{2}\overline{f}_z D_2^2 + A_2 D_2\overline{\tau},\\ &L_5 = A_2 D_1 D_2, \quad L_6 = \tfrac{1}{2}A_2 D_2^2. \end{aligned}\right\} \tag{3.6}$$

Formula (3.5) can be used to show that the flame height first decreases and then increases with the rotation speed. In this paper we are interested in fire whirls for which the rotation speed is not very high, so that the last four terms in (3.5) are small in comparison with the first three. To see that, we use two typical sets of parameters ($\omega = 1\,\mathrm{s}^{-1}$, $r_0 = 10\,\mathrm{m}$, $T_f = 1000\,\mathrm{K}$ and $\omega = 10\,\mathrm{s}^{-1}$, $r_0 = 1\,\mathrm{m}$, $T_f = 1000\,\mathrm{K}$, for it has been reported both experimentally and numerically that the faster the flame rotates, the thinner it becomes) to estimate the magnitude of the last four terms.

Note that

$$\frac{D_2}{\overline{\tau}} = \frac{r_0^2}{2RT_f}\left\{\frac{m\rho_{fuel}r_0^2\beta(T_f-T_0)}{4\rho_0}\frac{\displaystyle\int_0^{r_0}\left(1-\frac{r^2}{r_0^2}\right)B(r)r\,\mathrm{d}r}{\displaystyle\left[\int_0^{r_0}B(r)r\,\mathrm{d}r\right]^2}\frac{E}{E-1}-1\right\} \times\frac{1+\beta(T_f-T_0)}{\beta(T_f-T_0)},$$

$$\frac{D_2}{D_1} = \frac{r_0^2}{2RT_f}\frac{\overline{V}_{z0}}{k_1r_0}\left\{\frac{m\rho_{fuel}r_0^2\beta(T_f-T_0)}{4\rho_0}\frac{\displaystyle\int_0^{r_0}\left(1-\frac{r^2}{r_0^2}\right)B(r)r\,\mathrm{d}r}{\displaystyle\left[\int_0^{r_0}B(r)r\,\mathrm{d}r\right]^2}\frac{E}{E-1}-1\right\} \times\frac{1+\beta(T_f-T_0)}{\beta(T_f-T_0)},$$

$$\frac{A_2}{\overline{\overline{f}}_z} = \frac{r_0^2}{2RT_f}\left[1+\frac{1}{\beta(T_f-T_0)}\right].$$

For the first set ($\omega = 1\,\mathrm{s}^{-1}$, $r_0 = 10\,\mathrm{m}$, $T_f = 1000\,\mathrm{K}$), it can be estimated that $r_0^2/2RT_f \sim O(10^{-3})$, leading to

$$\frac{D_2}{\overline{\tau}} \sim \frac{D_2}{D_1} \sim \frac{A_2}{\overline{\overline{f}}_z} \sim O(10^{-3}).$$

Comparing corresponding terms of the coefficients given by (3.6), we obtain

$$\frac{L_3}{L_1} \sim O(10^{-3}), \quad \frac{L_5}{L_1} \sim O(10^{-6}), \quad \frac{L_4}{L_2} \sim O(10^{-3}), \quad \frac{L_6}{L_2} \sim O(10^{-9}), \tag{3.7}$$

and thus

$$\frac{L_3\omega^3}{L_1\omega} \sim O(10^{-3}), \quad \frac{L_5\omega^5}{L_1\omega} \sim O(10^{-6}), \quad \frac{L_4\omega^4}{L_2\omega^2} \sim O(10^{-3}), \quad \frac{L_6\omega^6}{L_2\omega^2} \sim O(10^{-9}). \tag{3.8}$$

For the second set ($\omega = 10\,\mathrm{s}^{-1}$, $r_0 = 1\,\mathrm{m}$, $T_f = 1000\,\mathrm{K}$), it can be estimated that $r_0^2/2RT_f \sim O(10^{-5})$, leading to

$$\frac{D_2}{\overline{\tau}} \sim \frac{D_2}{D_1} \sim \frac{A_2}{\overline{\overline{f}}_z} \sim O(10^{-5}).$$

Comparing corresponding terms of the coefficients given by (3.6), we obtain

$$\frac{L_3}{L_1} \sim O(10^{-5}), \quad \frac{L_5}{L_1} \sim O(10^{-10}), \quad \frac{L_4}{L_2} \sim O(10^{-5}), \quad \frac{L_6}{L_2} \sim O(10^{-15}), \tag{3.9}$$

and thus

$$\frac{L_3\omega^3}{L_1\omega} \sim O(10^{-3}), \quad \frac{L_5\omega^5}{L_1\omega} \sim O(10^{-6}), \quad \frac{L_4\omega^4}{L_2\omega^2} \sim O(10^{-3}), \quad \frac{L_6\omega^6}{L_2\omega^2} \sim O(10^{-11}). \tag{3.10}$$

Thus we see that the last four terms are negligible in comparison with the leading terms. Neglecting them does not affect the conclusion but makes the formula simpler.

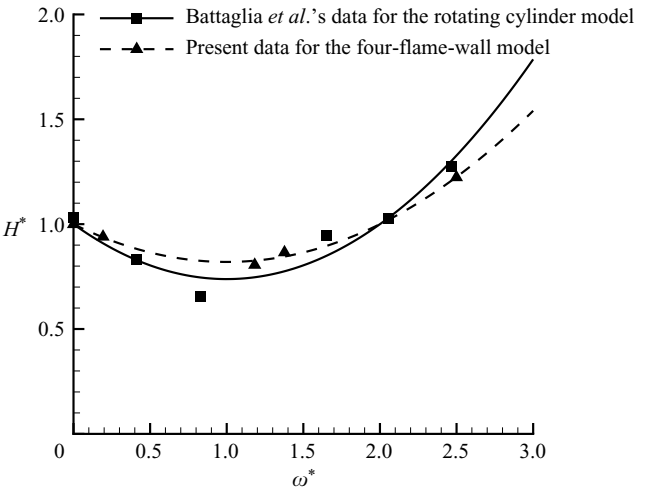

FIGURE 10. Dependence of the flame height on the rotation speed.

With the last terms neglected, (3.5) becomes

$$H \sim \overline{H} - L_1\omega + L_2\omega^2, \tag{3.11}$$

or

$$H \sim H_0 + L(\omega - \omega_0)^2, \tag{3.12}$$

where

$$L = L_2, \quad \omega_0 = \frac{L_1}{2L_2}, \quad H_0 = \overline{H} - \frac{L_1^2}{4L_2}.$$

From (3.12), it is clear that the flame height has a minimum value H_0 at $\omega = \omega_0$. The non-rotating flame height $\overline{H}$ in (3.11) and the minimum-height rotation speed ω_0 in (3.12) are two important parameters for fire whirls, which can be specified as the characteristic flame height and the characteristic rotation speed, respectively, to write the non-dimensional form of the expression relating the flame height to the rotation speed:

$$H^* = \frac{H}{\overline{H}}, \quad \omega^* = \frac{\omega}{\omega_0}, \quad H^* \sim H_0^* + L^*(\omega^* - 1)^2. \tag{3.13a–c}$$

Battaglia *et al.* (2000*a*) give results that indicate that the flame height decreases with whirl to a minimum before increasing again as the whirl increases further. The present model supports their findings. In figure 10 we display a comparison of the curve (3.13*c*) to the numerical results of Battaglia *et al.* (2000*a*), which have been non-dimensionalized by (3.13).

The above example is for a fire whirl generated by artificially imposing an angular momentum on a flame. Now we check if (3.13) can also be applied to the case of fire whirls produced due to surrounding flame sources. In figure 10 we also display a comparison of the curve (3.13*c*) to our numerical results for the four-flame-wall model with different gap fractions, which have been non-dimensionalized by (3.13). We still see that the flame height first decreases before increasing as the rotation speed increases.

3.1. *Role of the rotation speed in increasing the buoyancy force*

For the region outside the boundary layer, we consider an axisymmetric steady inviscid flow and write the governing equations in a cylindrical coordinate system as

$$\frac{\partial V_r}{\partial r} + \frac{V_r}{r} + \frac{\partial V_z}{\partial z} = 0, \tag{3.14a}$$

$$V_r \frac{\partial V_r}{\partial r} + V_z \frac{\partial V_r}{\partial z} - \frac{V_\theta^2}{r} = -\frac{1}{\rho}\frac{\partial p}{\partial r}, \tag{3.14b}$$

$$V_r \frac{\partial V_z}{\partial r} + V_z \frac{\partial V_z}{\partial z} = -\frac{1}{\rho}\frac{\partial p}{\partial z} - g. \tag{3.14c}$$

Here V_r, V_θ and V_z are respectively the radial (r), azimuthal (θ) and axial (z) velocity components, p is the pressure, ρ is the density and g is the gravitational acceleration.

First we consider a flame without rotation, i.e. $V_\theta = 0$. In that case the physical quantities are identified by an overbar and we have

$$\overline{V}_r \frac{\partial \overline{V}_r}{\partial r} + \overline{V}_z \frac{\partial \overline{V}_r}{\partial z} = -\frac{1}{\overline{\rho}}\frac{\partial \overline{p}}{\partial r}, \tag{3.15a}$$

$$\overline{V}_r \frac{\partial \overline{V}_z}{\partial r} + \overline{V}_z \frac{\partial \overline{V}_z}{\partial z} = -\frac{1}{\overline{\rho}}\frac{\partial \overline{p}}{\partial z} - g. \tag{3.15b}$$

Using the well-known Boussinesq approximation, (3.15b) can be rewritten as

$$\overline{V}_r \frac{\partial \overline{V}_z}{\partial r} + \overline{V}_z \frac{\partial \overline{V}_z}{\partial z} = \beta(T_f - T_0)g, \tag{3.16}$$

where β is the volume expansion coefficient. Along the centreline, we take $r = 0$ in (3.16) and note that $\overline{V}_r = 0$ at $r = 0$ so that the following equation holds along the centreline of the plume:

$$\overline{V}_z \frac{\partial \overline{V}_z}{\partial z} = \beta(T_f - T_0)g. \tag{3.17}$$

Here

$$\overline{V}_z \frac{\partial \overline{V}_z}{\partial z} = \frac{\mathrm{d}z}{\mathrm{d}t}\frac{\partial \overline{V}_z}{\partial z} = \frac{\mathrm{d}\overline{V}_z}{\mathrm{d}t},$$

thus

$$\frac{\mathrm{d}\overline{V}_z}{\mathrm{d}t} = \beta(T_f - T_0)g. \tag{3.18}$$

Fuel particles start from the top of the boundary layer at $t = 0$, which is assumed to be the beginning of the mixing-controlled combustion. Denoting the initial axial velocity as $\overline{V}_{z0}$ and integrating (3.18), we obtain

$$\overline{V}_z(t) = \frac{\mathrm{d}z}{\mathrm{d}t} = \beta(T_f - T_0)gt + \overline{V}_{z0}. \tag{3.19}$$

Integrating again yields

$$z(t) = \tfrac{1}{2}\beta(T_f - T_0)gt^2 + \overline{V}_{z0}t. \tag{3.20}$$

According to our assumption, the flame height $\overline{H}$ is obtained when t is equal to the rising time $\overline{\tau}$, so that

$$\overline{H} = z(\overline{\tau}) = \tfrac{1}{2}\beta(T_f - T_0)g\overline{\tau}^2 + \overline{V}_{z0}\overline{\tau}. \tag{3.21}$$

Now consider a rotating flame. By means of an order of magnitude estimation (see Appendix B), we show that (3.14) can be simplified to

$$\frac{1}{\rho}\frac{\partial p}{\partial r} \sim \omega^2 r, \tag{3.22a}$$

$$V_r\frac{\partial V_z}{\partial r} + V_z\frac{\partial V_z}{\partial z} \sim -\frac{1}{\rho}\frac{\partial p}{\partial z} - g. \tag{3.22b}$$

The flame region is assumed to be a cylinder of hot gas with a uniform temperature T_f. The pressure is related to the temperature through the equation of state

$$p = \rho R T_f. \tag{3.23}$$

Here R is the gas constant. Combining (3.23) and (3.22a) yields

$$\frac{RT_f}{\rho}\frac{\partial(\rho)}{\partial r} \sim \omega^2 r. \tag{3.24}$$

Integrating (3.24) results in

$$\rho \sim C\exp(\omega^2 r^2/2RT_f), \tag{3.25}$$

where C is a constant. We use the Boussinesq assumption to write

$$\rho\,|_{r=r_0} \sim \rho_0/[1+\beta(T_f - T_0)]. \tag{3.26}$$

Here r_0 is the edge of the rotating flame, assumed to have the same value for all z, ρ_0 is the background density and T_0 is the background temperature. Inserting (3.26) into (3.25), we obtain $C \sim \rho_0\exp(-\omega^2 r_0^2/2RT_f)/[1+\beta(T_f - T_0)]$. Hence the expression for the density is given by

$$\rho \sim \rho_0\exp\left(\omega^2\left(r^2 - r_0^2\right)/2RT_f\right)/[1+\beta(T_f - T_0)]. \tag{3.27}$$

The parameter $\omega^2(r^2 - r_0^2)/2RT_f$ is generally very small, so (3.27) can be written as

$$\rho = \overline{\rho} + \rho', \tag{3.28}$$

where

$$\overline{\rho} \sim \frac{\rho_0}{[1+\beta(T_f - T_0)]} \tag{3.29}$$

is the flame density in the case without rotation, and

$$\rho' \sim \frac{\rho_0\omega^2\left(r^2 - r_0^2\right)/2RT_f}{1+\beta(T_f - T_0)} \tag{3.30}$$

is the perturbation caused by rotation. Inserting (3.30) into (3.23), we obtain the perturbation pressure as follows:

$$p' \sim \frac{\rho_0\omega^2\left(r^2 - r_0^2\right)/2}{1+\beta(T_f - T_0)}. \tag{3.31}$$

Generally, for simple flame combustion without rotation, the spatial distribution of pressure is evaluated by the equation of hydrostatic equilibrium in an isotropic atmosphere as

$$\overline{p} = p_a - \rho_0 g z, \tag{3.32}$$

where p_a is the standard atmosphere pressure. The sum of (3.31) and (3.33) gives the pressure distribution inside the flame as

$$p \sim p_a - \rho_0 g z + \frac{\rho_0 \omega^2 \left(r^2 - r_0^2\right)/2}{1 + \beta(T_f - T_0)}. \tag{3.33}$$

Substituting (3.27), (3.31) and (3.33) into (3.22b) yields

$$V_r \frac{\partial V_z}{\partial r} + V_z \frac{\partial V_z}{\partial z} \sim \left\{\exp\left(-\omega^2\left(r^2 - r_0^2\right)\right)/2RT_f\right)[1 + \beta(T_f - T_0)] - 1\Big\} g. \tag{3.34}$$

The right-hand side of (3.34) is the buoyancy force inside the flame, an increasing function of ω. Taking $r = 0$ and thus $V_r = 0$ (along the centreline of the plume), we obtain

$$V_z \frac{\partial V_z}{\partial z} = \frac{\mathrm{d}V_z}{\mathrm{d}t} = f_z, \tag{3.35}$$

where

$$f_z \sim \exp\left(\omega^2 r_0^2/2RT_f\right)[1 + \beta(T_f - T_0)] - 1, \tag{3.36}$$

showing that along the centreline of the plume, the buoyancy force f_z acts to accelerate of the rising motion. Expanding (3.36) about $\omega^2 r_0^2/2RT_f$ results in

$$f_z \sim \overline{f}_z + A_2 \omega^2, \tag{3.37}$$

where

$$\overline{f}_z = \beta(T_f - T_0) g$$

is the buoyancy force in the case without rotation, and the square term of ω shows the increase of buoyancy force along the centreline of the plume due to rotation, with coefficient

$$A_2 = \frac{r_0^2}{2RT_f}[1 + \beta(T_f - T_0)] g.$$

Integrating (3.35) yields

$$V_z = f_z t + V_{z0}, \tag{3.38}$$

or

$$V_z = \sqrt{2 f_z z + V_{z0}^2}. \tag{3.39}$$

Again, integrating (3.38) yields

$$z = \tfrac{1}{2} f_z t^2 + V_{z0} t. \tag{3.40}$$

3.2. *Role of the rotation speed in reducing the initial vertical velocity*

For the boundary layer flow, the continuity equation and the Navier–Stokes equations are written in axisymmetric form as follows:

$$\frac{\partial V_r}{\partial r} + \frac{V_r}{r} + \frac{\partial V_z}{\partial z} = 0, \tag{3.41a}$$

$$V_r \frac{\partial V_r}{\partial r} + V_z \frac{\partial V_r}{\partial z} - \frac{V_\theta^2}{r} = -\frac{1}{\rho}\frac{\partial p}{\partial r} + \nu\left[\frac{\partial^2 V_r}{\partial r^2} + \frac{\partial}{\partial r}\left(\frac{V_r}{r}\right) + \frac{\partial^2 V_r}{\partial z^2}\right], \tag{3.41b}$$

$$V_r \frac{\partial V_\theta}{\partial r} + V_z \frac{\partial V_\theta}{\partial z} + \frac{V_r V_\theta}{r} = \nu\left[\frac{\partial^2 V_\theta}{\partial r^2} + \frac{\partial}{\partial r}\left(\frac{V_\theta}{r}\right) + \frac{\partial^2 V_\theta}{\partial z^2}\right], \tag{3.41c}$$

$$V_r\frac{\partial V_z}{\partial r}+V_z\frac{\partial V_z}{\partial z}=\frac{1}{\rho}\frac{\partial p}{\partial z}+\nu\left(\frac{\partial^2 V_z}{\partial r^2}+\frac{1}{r}\frac{\partial V_z}{\partial r}+\frac{\partial^2 V_z}{\partial z^2}\right)-g. \tag{3.41d}$$

To simplify, we non-dimensionalize equations (3.41) and ignore smaller terms based on order-of-magnitude estimations (see Appendix C). Eventually we obtain

$$V_r\frac{\partial V_r}{\partial r}+V_z\frac{\partial V_r}{\partial z}-\frac{V_\theta^2}{r}\sim\nu\frac{\partial^2 V_r}{\partial z^2}. \tag{3.42}$$

If no rotation occurs, there are only radial and axial velocity components, represented by $\overline{V}_r$ and $\overline{V}_z$, satisfying

$$\overline{V}_r\frac{\partial \overline{V}_r}{\partial r}+\overline{V}_z\frac{\partial \overline{V}_r}{\partial z}\sim\nu\frac{\partial^2 \overline{V}_r}{\partial z^2}. \tag{3.43}$$

Now we consider small perturbations caused by rotation, rewriting the radial and axial velocity components as $\overline{V}_r+V_r'$ and $\overline{V}_z+V_z'$, which satisfy

$$(\overline{V}_r+V_r')\frac{\partial(\overline{V}_r+V_r')}{\partial r}+(\overline{V}_z+V_z')\frac{\partial(\overline{V}_r+V_r')}{\partial z}-\frac{V_\theta^2}{r}\sim\nu\frac{\partial^2(\overline{V}_r+V_r')}{\partial z^2}. \tag{3.44}$$

Neglecting the small terms of second-order yields

$$\overline{V}_r\frac{\partial \overline{V}_r}{\partial r}+\overline{V}_r\frac{\partial V_r'}{\partial r}+V_r'\frac{\partial \overline{V}_r}{\partial r}+\overline{V}_z\frac{\partial \overline{V}_r}{\partial z}+\overline{V}_z\frac{\partial V_r'}{\partial z}+V_z'\frac{\partial \overline{V}_r}{\partial z}-\frac{V_\theta^2}{r}\sim\nu\frac{\partial^2 \overline{V}_r}{\partial z^2}+\nu\frac{\partial^2 V_r'}{\partial z^2}. \tag{3.45}$$

Using (3.43) to eliminate the terms without any perturbing quantity, we obtain

$$\overline{V}_r\frac{\partial V_r'}{\partial r}+V_r'\frac{\partial \overline{V}_r}{\partial r}+\overline{V}_z\frac{\partial V_r'}{\partial z}+V_z'\frac{\partial \overline{V}_r}{\partial z}-\frac{V_\theta^2}{r}\sim\nu\frac{\partial^2 V_r'}{\partial z^2}. \tag{3.46}$$

Similarly, from the continuity equation

$$\frac{\partial \overline{V}_r}{\partial r}+\frac{\overline{V}_r}{r}+\frac{\partial \overline{V}_z}{\partial z}=0 \tag{3.47}$$

and

$$\frac{\partial(\overline{V}_r+V_r')}{\partial r}+\frac{(\overline{V}_r+V_r')}{r}+\frac{\partial(\overline{V}_z+V_z')}{\partial z}=0, \tag{3.48}$$

we obtain

$$\frac{\partial V_r'}{\partial r}+\frac{V_r'}{r}+\frac{\partial V_z'}{\partial z}=0. \tag{3.49}$$

From (3.46) and (3.49), we obtain (see Appendix D)

$$V_r'\sim\frac{k_1\omega^2 r_0}{\nu}rz,\quad V_z'\sim-\frac{k_1\omega^2 r_0}{\nu}z^2. \tag{3.50}$$

On the top of the boundary layer, substituting $z=\delta$ into (3.50) yields

$$V_{z0}'=V_z'|_{z=\delta}\sim-\frac{k_1\omega^2 r_0}{\nu}\delta^2. \tag{3.51}$$

Using (C6), we have

$$\delta\sim\sqrt{\frac{r_0}{V_\Omega}\nu}=\sqrt{\frac{\nu}{\omega}}. \tag{3.52}$$

Inserting (3.52) into (3.51) yields

$$V_{z0}'\sim-k_1 r_0\omega, \tag{3.53}$$

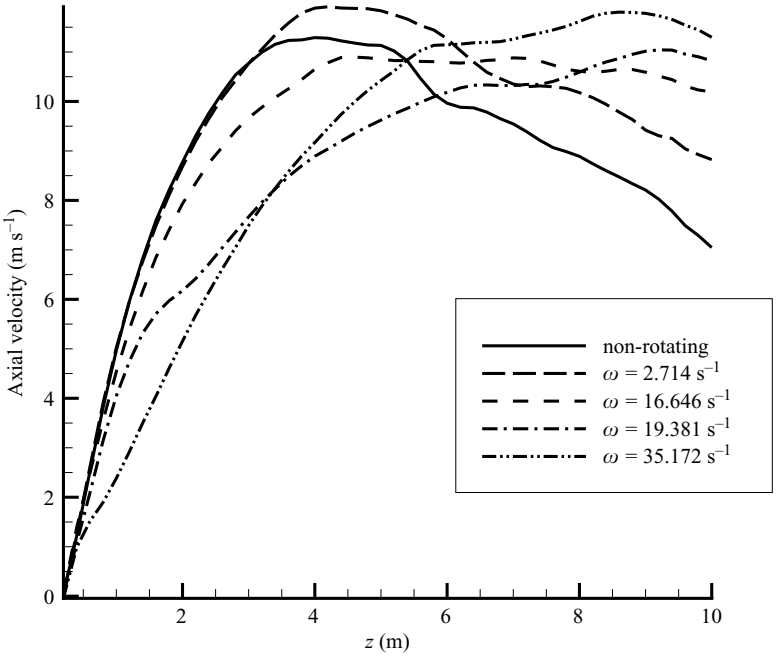

FIGURE 11. Vertical (axial) velocity along the centreline of the central flame for the four-flame-wall model.

and thus

$$V_{z0} \sim \overline{V}_{z0} - k_1 r_0 \omega, \tag{3.54}$$

showing that the rotation reduces the initial vertical velocity due to the viscous layer.

It should be emphasized that the division into an inviscid part and a viscous part is essential to our analysis. In order to show what is happening, we display in figure 11 the vertical velocity along the centreline of the main flame for different rotation speeds (by using different gap fractions for the four-flame-wall model). It is seen that for the bottom of the viscous-dominated part of the flame, the vertical velocity decreases with the rotation speed, while for the upper or buoyancy-dominated part, the vertical velocity is an increasing function of the rotation speed.

3.3. *Role of the rotation speed in first shortening then extending the rising time*

According to § 3.1, the buoyancy force along the centreline of the plume is

$$f_z \sim \left\{\exp\left(\omega^2 r_0^2 / 2RT_f\right)[1 + \beta(T_f - T_0)] - 1\right\} g. \tag{3.55}$$

Thus, the axial velocity is

$$V_z = f_z t + V_{z0}, \tag{3.56}$$

where, according to § 3.2,

$$V_{z0} \sim \overline{V}_{z0} - k_1 r_0 \omega. \tag{3.57}$$

We assume the following expression for the whole space:

$$\hat{V}_z = B(r)(f_z t + V_{z0}), \quad \hat{V}_{z0} = B(r) V_{z0}, \tag{3.58}$$

where $B(r)$ is an unknown non-dimensional function of r, satisfying $B(0)=1$. For a section of flame with height z above the boundary layer, the following equation holds due to mass conservation:

$$\int_0^{r_0} \rho(r)(\hat{V}_z - \hat{V}_{z0})2\pi r \,\mathrm{d}r = \rho(r_0)V_{ent}\, 2\pi r_0 z. \tag{3.59}$$

Here V_{ent} is height-averaged entrainment velocity, and $\rho(r)$ is given by (see § 3.1)

$$\rho(r) \sim \rho_0 \exp\left(\omega^2\left(r^2 - r_0^2\right)\right)/2RT_f/[1+\beta(T_f - T_0)]. \tag{3.60}$$

Inserting (3.58) into (3.59) yields

$$V_{ent} = \frac{\displaystyle\int_0^{r_0} \rho(r)B(r)r\,\mathrm{d}r}{r_0\rho(r_0)} \frac{V_z - V_{z0}}{z} = \frac{\displaystyle\int_0^{r_0} \rho(r)B(r)r\,\mathrm{d}r}{r_0\rho(r_0)} \frac{f_z t}{\frac{1}{2}f_z t^2 + V_{z0}t}. \tag{3.61}$$

The role of the rotation speed in the height-averaged entrainment velocity, represented by (3.61), will be made clear in Appendix E. Using (3.61), the total mass of entrained air can be written as

$$\begin{aligned} Q_{air} &= \int_0^{\tau} \rho(r_0)V_{ent}\, 2\pi r_0 H \,\mathrm{d}t \\ &= 2\pi H \int_0^{r_0} \rho(r)B(r)r\,\mathrm{d}r \int_0^{\tau} \frac{f_z t}{\frac{1}{2}f_z t^2 + V_{z0}t}\,\mathrm{d}t \\ &= 4\pi H \int_0^{r_0} \rho(r)B(r)r\,\mathrm{d}r \ln\frac{\frac{1}{2}f_z\tau + V_{z0}}{V_{z0}}. \end{aligned} \tag{3.62}$$

On the other hand, the mass of fuel inside the flame is

$$Q_{fuel} = \rho_{fuel}\pi r_0^2 H, \tag{3.63}$$

where ρ_{fuel} is the averaged density of fuel gas inside the flame. The stoichiometric ratio of fuel to air is $1:m$, i.e.

$$Q_{air} = m\,Q_{fuel}. \tag{3.64}$$

Inserting (3.62) and (3.63) into (3.64), we obtain the rising time as

$$\tau = \left\{ \exp\left[\frac{m\rho_{fuel}r_0^2}{4\displaystyle\int_0^{r_0} \rho(r)B(r)r\mathrm{d}r} \right] - 1 \right\} \frac{2V_{z0}}{f_z}, \tag{3.65}$$

Substituting (3.55), (3.57) and (3.60) into (3.65) and expanding the exponential function about $\omega^2 r_0^2/2RT_f$, we obtain

$$\tau \sim \overline{\tau} - D_1\omega + D_2\omega^2, \tag{3.66}$$

where

$$\overline{\tau} = (E-1)\frac{\overline{V}_{z0}}{\beta(T_f - T_0)g}$$

is the rising time in the case without rotation, and the series of terms of ω represent the influence of rotation on the rising time, with coefficients

$$D_1 = (E-1)\,\frac{k_1 r_0}{\beta(T_f - T_0)g},$$

$$D_2 = \frac{r_0^2 \overline{V}_{z0}}{2RT_f}\left\{\frac{m\rho_{fuel} r_0^2 \beta(T_f - T_0)}{4\rho_0}\,\frac{\displaystyle\int_0^{r_0}\left(1-\frac{r^2}{r_0^2}\right)B(r)r\,\mathrm{d}r}{\left[\displaystyle\int_0^{r_0} B(r)r\,\mathrm{d}r\right]^2}E - E + 1\right\} \times \frac{1+\beta(T_f - T_0)}{\beta^2(T_f - T_0)^2 g}.$$

In the above expressions, E is a parameter given by

$$E = \exp\left\{\frac{m\rho_{fuel} r_0^2[1+\beta(T_f - T_0)]}{4\rho_0 \displaystyle\int_0^{r_0} B(r)r\,\mathrm{d}r}\right\}.$$

Clearly $E > 1$ and thus $D_1 > 0$. Now we shall prove that D_2 is a positive number. Let

$$\gamma = \frac{m\rho_{fuel} r_0^2}{4\rho_0},$$

and the terms within curly brackets of the expression for D_2 can be rewritten as

$$\Gamma(\gamma) = \left\{\frac{\beta(T_f - T_0)\displaystyle\int_0^{r_0}\left(1-\frac{r^2}{r_0^2}\right)B(r)r\,\mathrm{d}r}{\left[\displaystyle\int_0^{r_0} B(r)r\,\mathrm{d}r\right]^2}(\gamma - 1)\right\}\exp\left\{\frac{[1+\beta(T_f - T_0)]}{\displaystyle\int_0^{r_0} B(r)r\,\mathrm{d}r}\gamma\right\} + 1. \tag{3.67}$$

It is easy to see that $\Gamma(\gamma)$ is an increasing function of γ, which means that $\Gamma(\gamma) > 0$ as $\gamma > 0$, and thus $D_2 > 0$. Now from (3.66) it is clear that the rising time first decreases before increasing as the rotation speed increases, due to the height-averaged entrainment velocity varying inversely (see Appendix E). In figure 12, we display a comparison of the curve (3.66) to data calculated by our numerical results for the four-flame-wall model with different gap fractions, showing that our analysis is correct.

4. Concluding remarks

In this paper, we have used numerical simulation, experimental observation and simplified physical analysis to study fire whirls and obtained the following conclusions:

(i) Rotation of a flame can be produced by surrounding flames which partially block the inward air stream and favour flows of the main flame in a particular circumferential direction. Unlike a solid wall, the flame wall weakens the momentum of the air stream entrained by the main flame due to the vertical motion inside the surrounding flames. Both regularly distributed and randomly distributed flame sources may induce rotation if they are placed asymmetrically in such a way as to have gaps favouring flows in a given circumferential direction.

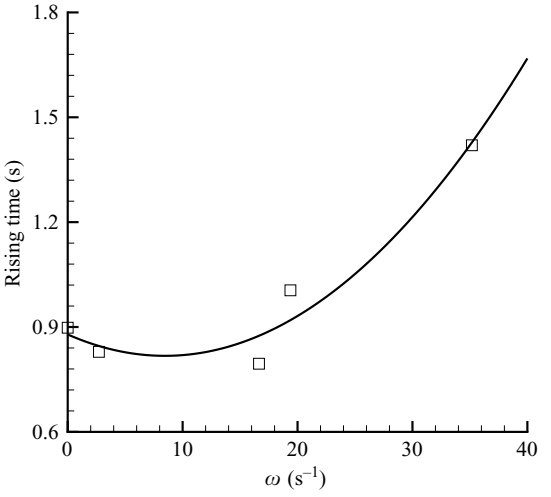

FIGURE 12. Dependence of the rising time on the rotation speed. Symbols: present data. Line: the fitted curve (3.66).

(ii) This rotation is absent if the surrounding flames are removed (gap fraction equal to 1) or if they form a closed polygonal flame (gap fraction equal to 0). For regularly distributed sources, the rotation speed is found to be highest if the gap fraction is close to 1/2, because for a gap fraction higher than this value, the additional air stream through the gaps contributes an angular momentum in such a direction as to oppose rotation. For irregularly distributed sources, no general criteria have been found in the present study.

(iii) The flame height H increases substantially due to rotation for large rotation speed while it decreases for small rotation speed. For large rotation speed, the rotation decreases the pressure thus increases the buoyancy force inside the flame. Also, the rotation suppresses the entrainment thereby slowing the rate of air/fuel mixing. For particular rising time, a rapid rising fuel particle can reach a higher altitude, thus the flame height increases with rotation. For low rotation speed, the initial vertical velocity of the flame, controlled by the boundary layer, is a decreasing function of the rotation speed. On the other hand, the rotation enhances the entrainment and speeds up the rate of air/fuel mixing, thus the rising time is shortened. Both cause the flame to decrease with swirling for small rotation speed.

In the present study, the quantitative relationship between the momentum reduction and the characteristics of the surrounding flame wall was not considered, but with such quantitative information, we could construct useful models to predict the rotation speed for a given source distributions. This could be a subject for future study.

A second subject deserving further study is the fire whirl for very high rotation speed, not considered here. For very high rotation speed, the flame becomes highly unstable. Under these conditions the flame shortens and smoke is formed (Chigier *et al.* 1970).

This work has been supported by the China NKBRSF project No. 2001CB409600. The authors are grateful to the referees for providing them with new materials, suggestions and help which proved to be very important while expanding and improving this work.

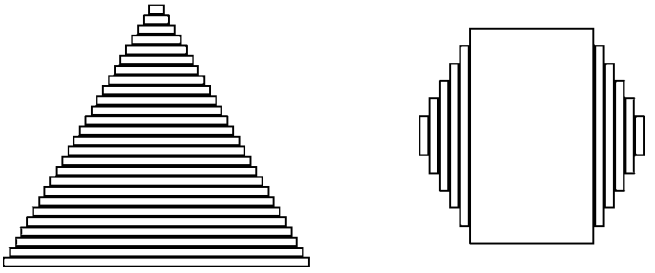

FIGURE 13. (*a*) The triangle and (*b*) hexagon centred pools made up of small blocks conforming with the underlying grid.

Appendix A. Numerical simulation method

The numerical simulations are performed by using the fire dynamics simulator (FDS) code (McGrattan 2004). To simulate fires of multiple flame sources, we have adapted the software to consider fire pools of any shape. Below we first outline the basic FDS tool, then we give the details related to our computations.

A.1. *Basic numerical method*

FDS is a computational fluid dynamics (CFD) model of fire-driven flow, developed by NIST, USA, whose codes are in the public domain. It solves the form of the Navier–Stokes equations appropriate for low-speed, thermally driven flow with emphasis on smoke and heat transport from fires by means of large-eddy simulation. The subgrid-scale motions are modelled by the Smagorinsky model. The core algorithm of the FDS is an explicit predictor–corrector scheme, second-order accurate in space and time. For most applications, FDS uses a mixture fraction combustion model, which assumes that combustion is mixing-controlled, and that the reaction of fuel and oxygen is infinitely fast.

A.2. *Specific methods and conditions used in the present computations*

In our computations, the computational domain is $10.0\,\mathrm{m} \times 10.0\,\mathrm{m} \times 10.0\,\mathrm{m}$. The origin of the Cartesian coordinate system is at the centre of the base central pool. For the four-wall model, the central fuel pool has size $2.0\,\mathrm{m} \times 2.0\,\mathrm{m} \times 0.2\,\mathrm{m}$ and the surrounding four rectangular fuel pools are of uniform size $3.5\,\mathrm{m} \times 0.5\,\mathrm{m} \times 0.2\,\mathrm{m}$.

The geometrical shapes of the central fuel pools are designed to fit the number of surrounding pools, e.g. a regular triangle for three pools, square for four pools and regular hexagon for six pools, with each side length D_3, D_4 and D_6, satisfying $D_3^2 = \sqrt{3}D_4^2/4 = 6D_6^2$ to ensure the same area of the central pool (here $4.0\,\mathrm{m}^2$). All the surrounding pools are the same width of 0.5 m, and the gap width is fixed at 1 m in all cases. Unfortunately, not all fuel pools can be precisely modelled in a simulation because FDS approximates the governing equations on a rectilinear grid and the user has to prescribe rectangular obstructions that must conform with the underlying grid. In order to solve this problem, we represent each shape, such as triangle or hexagon, by a number of small regular blocks of rectangular shape as shown in figure 13. Such a method is accurate when this number is large enough.

In all the simulations, the heat release rate per unit area (HRRPUA), which represents the fire combustion intensity, is fixed at $2000\,\mathrm{kW\,m^{-2}}$. The boundary condition for the floor of the computational domain is that of a cold inert wall. For the ceiling and the four side surfaces an open condition is used to describe a passive opening to the exterior atmosphere.

Appendix B. Simplification of the Euler equations of the boundary layer

The flame diameter σ is assumed to be much smaller than the flame height H. We use the flame height H as the characteristic length and the velocity $V_H = V_z|_{z=H}$ as the characteristic velocity, and define the following non-dimensional quantities:

$$r^* = \frac{r}{H}, \quad z^* = \frac{z}{H}, \quad \sigma^* = \frac{\sigma}{H}, \quad V_r^* = \frac{V_r}{V_H}, \quad V_z^* = \frac{V_z}{V_H}, \quad p^* = \frac{p}{\rho V_H^2}. \tag{B 1}$$

Multiplying (3.14*a*) by H/V_H and (3.14*b*, *c*) by H/V_H^2, we use the non-dimensional quantities defined by (B 1) and rewrite equations (3.14) as follows:

$$\underset{1}{\frac{\partial V_r^*}{\partial r^*}} + \underset{1}{\frac{V_r^*}{r^*}} + \underset{1}{\frac{\partial V_z^*}{\partial z^*}} = 0, \tag{B 2a}$$

$$\underset{\sigma^* \cdot 1}{V_r^* \frac{\partial V_r^*}{\partial r^*}} + \underset{1 \cdot \sigma^*}{V_z^* \frac{\partial V_r^*}{\partial z^*}} - \underset{\frac{1}{\sigma^*}}{\frac{V_\theta^{*2}}{r^*}} = \underset{\frac{1}{\sigma^*}}{-\frac{\partial p^*}{\partial r^*}}, \tag{B 2b}$$

$$\underset{\sigma^* \cdot \frac{1}{\sigma^*}}{V_r^* \frac{\partial V_z^*}{\partial r^*}} + \underset{1 \cdot 1}{V_z^* \frac{\partial V_z^*}{\partial z^*}} = \underset{1}{-\frac{\partial p^*}{\partial z^*}} - \underset{1}{\frac{H}{V_H^2} g}, \tag{B 2c}$$

The estimated order of magnitude of the terms in (B 2), noting them below them are noted. Since $\sigma^* = \sigma/H$ is a small quantity, with r being between 0 and $\sigma/2$, and z being between 0 and H, we have the following estimations:

$$r^* = \frac{r}{H} \sim O(\sigma^*), \quad z^* = \frac{z}{H} \sim O(1), \tag{B 3}$$

$$V_z^* = \frac{V_z}{V_H} \sim O(1). \tag{B 4}$$

The continuity equation (B 2*a*) shows that the order of V_r^* is smaller than that of V_z^*, therefore

$$V_r^* \sim O(\sigma^*). \tag{B 5}$$

Estimations for the velocity derivatives in the non-dimensional equations (B 2) are

$$\left.\begin{aligned} &\frac{\partial V_r^*}{\partial r^*} \sim O(1), \quad \frac{\partial V_r^*}{\partial z^*} \sim O(\sigma^*), \quad \frac{\partial V_z^*}{\partial r^*} \sim O\left(\frac{1}{\sigma^*}\right), \\ &\frac{\partial V_z^*}{\partial r^*} \sim O\left(\frac{1}{\sigma^*}\right), \quad \frac{\partial V_z^*}{\partial z^*} \sim O(1). \end{aligned}\right\} \tag{B 6}$$

Reserving the primary terms in equation (B 2*b*, *c*), we have

$$-\frac{V_\theta^{*2}}{r^*} \sim -\frac{\partial p^*}{\partial r^*}, \tag{B 7a}$$

$$V_r^* \frac{\partial V_z^*}{\partial r^*} + V_z^* \frac{\partial V_z^*}{\partial z^*} \sim -\frac{\partial p^*}{\partial z^*} - \frac{H}{V_H^2} g, \tag{B 7b}$$

or in dimensional form (using $V_\theta = \omega r$, where ω is the angular velocity of the flame):

$$\frac{1}{\rho}\frac{\partial p}{\partial r} \sim \omega^2 r, \tag{B 8a}$$

$$V_r\frac{\partial V_z}{\partial r} + V_z\frac{\partial V_z}{\partial z} \sim -\frac{1}{\rho}\frac{\partial p}{\partial z} - g. \tag{B 8b}$$

Appendix C. Simplification of the Navier–Stokes equations in the boundary layer

Specifying the flame radius r_0 as the characteristic length and the maximum rotation speed $V_\Omega = \omega r_0$ as the characteristic speed, and denoting the boundary layer thickness as δ, we define the following non-dimensional quantities:

$$r^* = \frac{r}{r_0}, \quad z^* = \frac{z}{r_0}, \quad \delta^* = \frac{\delta}{r_0}, \qquad V_r^* = \frac{V_r}{V_\Omega}, \quad V_z^* = \frac{V_z}{V_\Omega}, \quad p^* = \frac{p}{\rho V_\Omega^2}. \tag{C 1}$$

Multiplying (3.41a) by r_0/V_Ω and (3.41b–d) by r_0/V_Ω^2, we use the non-dimensional quantities defined by (C 1) and rewrite equations (3.41) in non-dimensional form as follows:

$$\underset{1}{\frac{\partial V_r^*}{\partial r^*}} + \underset{1}{\frac{V_r^*}{r^*}} + \underset{1}{\frac{\partial V_z^*}{\partial z^*}} = 0, \tag{C 2a}$$

$$\underset{1\cdot 1}{V_r^*\frac{\partial V_r^*}{\partial r^*}} + \underset{\delta^*\cdot\frac{1}{\delta^*}}{V_z^*\frac{\partial V_r^*}{\partial z^*}} - \underset{1}{\frac{V_\theta^{*2}}{r^*}} = -\underset{\delta^*}{\frac{\partial p^*}{\partial r^*}} + \frac{1}{Re}\left[\underset{\delta^{*2}}{\frac{\partial^2 V_r^*}{\partial r^{*2}}} + \underset{1}{\frac{\partial}{\partial r^*}\left(\frac{V_r^*}{r^*}\right)} + \underset{\frac{1}{\delta^{*2}}}{\frac{\partial^2 V_r^*}{\partial z^{*2}}}\right], \tag{C 2b}$$

$$\underset{1\cdot 1}{V_r^*\frac{\partial V_\theta^*}{\partial r^*}} + \underset{\delta^*\cdot\frac{1}{\delta^*}}{V_z^*\frac{\partial V_\theta^*}{\partial z^*}} + \underset{1}{\frac{V_r^* V_\theta^*}{r^*}} = \frac{1}{Re}\left[\underset{\delta^{*2}}{\frac{\partial^2 V_\theta^*}{\partial r^{*2}}} + \underset{1}{\frac{\partial}{\partial r^*}\left(\frac{V_\theta^*}{r^*}\right)} + \underset{\frac{1}{\delta^{*2}}}{\frac{\partial^2 V_\theta^*}{\partial z^{*2}}}\right], \tag{C 2c}$$

$$\underset{1\cdot\delta^*}{V_r^*\frac{\partial V_z^*}{\partial r^*}} + \underset{\delta^*\cdot 1}{V_z^*\frac{\partial V_z^*}{\partial z^*}} = -\underset{1}{\frac{\partial p^*}{\partial z^*}} + \frac{1}{Re}\left(\underset{\delta^{*2}}{\frac{\partial^2 V_z^*}{\partial r^{*2}}} + \underset{\delta^*}{\frac{1}{r^*}\frac{\partial V_z^*}{\partial r^*}} + \underset{1\cdot\delta^*}{\frac{\partial^2 V_z^*}{\partial z^{*2}}}\right) - \underset{1}{\frac{r_0}{V_\Omega^2}g}, \tag{C 2d}$$

where $Re = V_\Omega r_0/\nu$ is the Reynolds number.

Again the order of magnitude of the terms in (C 2), are given below them. By assumption, $\delta^* = \delta/r_0$ is a small quantity. In the boundary layer, r being between 0 and r_0, z being between 0 and δ, V_θ being between 0 and V_Ω, we have the following estimations:

$$r^* = \frac{r}{r_0} \sim O(1), \quad z^* = \frac{z}{r_0} \sim O(\delta^*), \quad V_\theta^* = \frac{V_\theta}{V_\Omega} \sim O(1). \tag{C 3}$$

The continuity equation (C 2a) shows that the order of V_z^* is smaller than that of V_r^*, therefore

$$V_r^* \sim O(1), \quad V_z^* \sim O(\delta^*). \tag{C 4}$$

Estimations for the velocity derivatives in the non-dimensional equations (C 2) are

$$\left.\begin{aligned}
&\frac{\partial V_r^*}{\partial r^*} \sim O(1),\ \frac{\partial^2 V_r^*}{\partial r^{*2}} \sim O(1),\ \frac{\partial}{\partial r^*}\left(\frac{V_r^*}{r^*}\right) \sim O(1),\ \frac{\partial V_r^*}{\partial z^*} \sim O\left(\frac{1}{\delta^*}\right),\ \frac{\partial^2 V_r^*}{\partial z^{*2}} \sim O\left(\frac{1}{\delta^{*2}}\right),\\
&\frac{\partial V_\theta^*}{\partial r^*} \sim O(1),\ \frac{\partial^2 V_\theta^*}{\partial r^{*2}} \sim O(1),\ \frac{\partial}{\partial r^*}\left(\frac{V_\theta^*}{r^*}\right) \sim O(1),\ \frac{\partial V_\theta^*}{\partial z^*} \sim O\left(\frac{1}{\delta^*}\right),\ \frac{\partial^2 V_\theta^*}{\partial z^{*2}} \sim O\left(\frac{1}{\delta^{*2}}\right),\\
&\frac{\partial V_z^*}{\partial r^*} \sim O(\delta^*),\ \frac{\partial^2 V_z^*}{\partial r^{*2}} \sim O(\delta^{*2}),\ \frac{\partial V_z^*}{\partial z^*} \sim O(1),\ \frac{\partial^2 V_z^*}{\partial z^{*2}} \sim O(1).
\end{aligned}\right\} \tag{C 5}$$

Equation (C 2*c*) shows the equilibrium between the inertial forces and the viscosity forces. The orders of the inertial terms have been estimated as 1 while that of the maximum viscosity term $\partial^2 V_\theta^*/\partial z^{*2}$ has been estimated as $O(1/\delta^{*2})$, which when multiplied by $1/Re$ should equal $O(1)$, i.e.

$$\frac{1}{Re}\frac{1}{\delta^{*2}} \sim O(1),$$

so

$$\frac{1}{Re} \sim O(\delta^{*2}). \tag{C 6}$$

In equation (C 2*d*), the inertial terms and the viscosity terms are all of small magnitude, implying that the pressure term has to equal the gravity term, whose order is 1, i.e.

$$\frac{\partial p^*}{\partial z^*} \sim O(1), \tag{C 7}$$

and thus,

$$\frac{\partial p^*}{\partial r^*} \sim O(\delta^*). \tag{C 8}$$

Reserving the primary terms in equation (C 2*b*), we have

$$V_r^*\frac{\partial V_r^*}{\partial r^*} + V_z^*\frac{\partial V_r^*}{\partial z^*} - \frac{V_\theta^{*2}}{r^*} \sim \frac{1}{Re}\frac{\partial^2 V_r^*}{\partial z^{*2}}, \tag{C 9}$$

or in dimensional form:

$$V_r\frac{\partial V_r}{\partial r} + V_z\frac{\partial V_r}{\partial z} - \frac{V_\theta^2}{r} \sim \nu\frac{\partial^2 V_r}{\partial z^2}. \tag{C 9b}$$

Appendix D. Solution of the perturbation equations in the boundary layer

We have obtained in § 3.2 the following equations for the perturbing velocity components:

$$\overline{V}_r\frac{\partial V_r'}{\partial r} + V_r'\frac{\partial \overline{V}_r}{\partial r} + \overline{V}_z\frac{\partial V_r'}{\partial z} + V_z'\frac{\partial \overline{V}_r}{\partial z} - \frac{V_\theta^2}{r} = \nu\frac{\partial^2 V_r'}{\partial z^2}. \tag{D 1a}$$

$$\frac{\partial V_r'}{\partial r} + \frac{V_r'}{r} + \frac{\partial V_z'}{\partial z} = 0. \tag{D 1b}$$

The rotation speed V_θ is in direct proportion to ωr, i.e. $V_\theta \sim \omega r$, thus

$$\frac{V_\theta^2}{r} \sim \omega^2 r. \tag{D 2}$$

Note that $\overline{V}_r$ and $\overline{V}_z$ are independent of ω in equation (D 1a), so we must have

$$V_r' \sim \omega^2, \quad V_z' \sim \omega^2. \tag{D 3}$$

Based on the standard dimensional analysis, V_r' has the following expression:

$$V_r' \sim \pm\frac{\omega^2 r^n r_0^{3-n}}{\nu} f(z^*), \quad n = 0, 1, 2, 3. \tag{D 4}$$

Here $z^* = z/r_0$ is a non-dimensional variable and $f(z^*)$ is an unknown non-dimensional function. In order to determine the index n, we substitute (D 4) into (D 1b) to obtain

$$V_z' \sim \frac{(n+1)\omega^2 r^{n-1} r_0^{3-n}}{\nu} \int f(z^*)\,\mathrm{d}z. \tag{D 5}$$

V_z can be neither zero nor infinite at $r = 0$, so we must have $n = 1$ and thus

$$V_r' \sim \pm\frac{\omega^2 r r_0^2}{\nu} f(z^*). \tag{D 6}$$

Since $z^* \sim O(\delta^*)$ is a small quantity, the use of Taylor's expansion leads to

$$V_r' \sim \pm\frac{\omega^2 r r_0^2}{\nu}(k_0 + k_1 z^* + k_2 z^{*2} + \cdots), \tag{D 7}$$

where $k_0, k_1, k_2, \ldots$ are non-dimensional coefficients. With the non-slip boundary condition $V_r'\,|_{z=0} = 0$, the constant k_0 is determined to be zero. Furthermore, substituting the following boundary conditions into equation (D 1a):

$$z = 0, \quad \overline{V}_r = V_r' = \overline{V}_z = V_z' = V_\theta = 0, \tag{D 8}$$

we obtain

$$z = 0, \quad \frac{\partial^2 V_r'}{\partial z^2} = 0, \tag{D 9}$$

which implies $k_2 = 0$. Neglecting the terms of order higher than $O(r^{*2})$ in (D 7), we have

$$V_r' \sim \pm\frac{k_1 \omega^2 r_0}{\nu} r z. \tag{D 10}$$

Inserting (D 10) into (D 1b) yields

$$V_z' \sim \mp\frac{k_1 \omega^2 r_0}{\nu} z^2, \tag{D 11}$$

which satisfies the boundary condition $V_z'\,|_{z=0} = 0$.

Now we determine whether the perturbing velocity components are positive or negative. If no rotation occurs, the air flows towards the central axis and rises up it, i.e.

$$\overline{V}_r < 0, \quad \overline{V}_z > 0.$$

When the flame is rotating, the centrifugal force acts on the system, doing negative work to reduce the kinetic energy. As the velocity changes, the work done by each force changes, and the velocity reaches a new balance. The kinetic energy also reduces If

$$V_r' \sim \frac{k_1 \omega^2 r_0}{\nu} r z, \quad V_z' \sim -\frac{k_1 \omega^2 r_0}{\nu} z^2, \tag{D 12a}$$

both V_r and V_z decrease. If

$$V_r' \sim -\frac{k_1\omega^2 r_0}{\nu} rz, \quad V_z' \sim \frac{k_1\omega^2 r_0}{\nu} z^2, \tag{D 12b}$$

both V_r and V_z increase. Obviously only the former is rational.

Appendix E. Role of rotation in first enhancing then suppressing the entrainment

We have the following expression for the height-averaged entrainment velocity derived in § 3.3:

$$V_{ent} = \frac{\int_0^{r_0} \rho(r)B(r)r\,\mathrm{d}r}{r_0\rho(r_0)} \cdot \frac{V_z - V_{z0}}{z}. \tag{E 1}$$

where (see § 3.1)

$$V_z = \sqrt{2f_z z + V_{z0}^2}. \tag{E 2}$$

Substituting (E 2) into (E 1), we obtain

$$V_{ent} = \frac{\int_0^{r_0} \rho(r)B(r)r\,\mathrm{d}r}{r_0\rho(r_0)} \frac{\sqrt{2f_z z + V_{z0}^2} - V_{z0}}{z}. \tag{E 3}$$

Roughly, (E 3) can be simplified as

$$V_{ent} = \frac{\int_0^{r_0} \rho(r)B(r)r\,\mathrm{d}r}{r_0\rho(r_0)} \frac{\sqrt{2f_z z}}{z}. \tag{E 4}$$

Inserting (3.55) and (3.60) into (E 4) and expanding the exponential function about $\omega^2 r_0^2/2RT$ yields

$$V_{ent} \sim \overline{V}_{ent} + J_2\omega^2 - J_4\omega^4, \tag{E 5}$$

where

$$\overline{V}_{ent} = \frac{\sqrt{\beta(T_f - T_0)g}}{r_0} \int_0^{r_0} B(r)r\,\mathrm{d}r$$

is the height-averaged entrainment velocity in the case without rotation, and the series of terms of ω represent the influence of rotation on entrainment, with coefficients as follows:

$$J_2 = \frac{r_0^2}{2RT_f} \frac{\sqrt{\beta(T_f - T_0)g}}{r_0} \left\{ \left[1 + \frac{1}{\beta(T_f - T_0)}\right] \int_0^{r_0} B(r)r\,\mathrm{d}r - \int_0^{r_0} \left(1 - \frac{r^2}{r_0^2}\right) B(r)r\,\mathrm{d}r \right\},$$

$$J_4 = \frac{r_0^2}{2RT_f} \frac{\sqrt{\beta(T_f - T_0)g}}{r_0} \left[1 + \frac{1}{\beta(T_f - T_0)}\right] \int_0^{r_0} \left(1 - \frac{r^2}{r_0^2}\right) B(r)r\,\mathrm{d}r.$$

Obviously J_4 is a positive number, and

$$\int_0^{r_0} \left(1 - \frac{r^2}{r_0^2}\right) B(r)r\,\mathrm{d}r < \int_0^{r_0} B(r)r\,\mathrm{d}r$$

leads to $J_2 > 0$. So (E 5) shows that the rotation enhances the entrainment first before later suppressing it. In order to check the relationship between rotation and

Rotation speed (s^{-1})	0	2.714	16.646	19.381	35.172
Entrainment velocity flux ($m^2\,s^{-1}$) at $z = 1\,m$	5.730	8.249	12.158	13.037	11.083
Entrainment velocity flux ($m^2\,s^{-1}$) at $z = 2\,m$	5.400	8.748	11.612	11.416	9.731
Entrainment velocity flux ($m^2\,s^{-1}$) at $z = 3\,m$	5.438	9.843	11.232	10.094	9.003

TABLE 4. The influence of the rotation speed on the entrainment velocity flux.

entrainment, we use our numerical results to calculate the entrainment velocity flux (i.e. the sum of entrainment velocities along the perimeter of the enclosure) at $z = 1\,m$, $z = 2\,m$ and $z = 3\,m$ for different rotation speeds, as listed in table 4. It is easy to see that the entrainment is first enhanced and then suppressed as the rotation speed increases.

REFERENCES

ATOBILOYE, R. Z. & BRITTER, R. E. 1994 On flame propagation along vortex tubes. *Combust. Flame* **98**, 220–230.

BATTAGLIA, F., MCGRATTAN, K. B., RHEM, R. G & BAUM, H. R. 2000*a* Simulating fire whirls. *Combust. Theory Model.* **4**, 123–138.

BATTAGLIA, F., REHM, R. G. & BAUM, H. R. 2000*b* The fluid mechanics of fire whirls: An inviscid model. *Phys. Fluids* **12**, 2859–2867.

CHIGIER, N. A., BEER, J. M., GRECOV, D. & BASSINDALE, K. 1970 Jet flames in rotating flow fields. *Combust. Flame* **14**, 171–180.

CHOW, W. K. & YIN, R. 2004 A new model on simulating smoke transport with computational fluid dynamics. *Building Environ.* **39**, 611–620.

CHOW, W. K. & ZOU, G. W. 2005 Correlation equations on fire-induced air flow rates through doorway derived by large eddy simulation. *Building Environ.* **40**, 897–906.

CHRISTENSEN, A. M. & ICOVE, D. J. 2004 The application of nist's fire dynamics simulator to the investigation of carbon monoxide exposure in the deaths of three pittsburgh fire fighters. *J. Forensic Sci.* **49**, 104–107.

EMMONS, H. W. & YING, S. J. 1967 The fire whirl. In *Proc. 11th Int. Symp. Combustion*, pp. 475–488. Combustion Institute, Pittsburgh, PA.

FAROUK, B., MCGRATTAN, K. B. & REHM, R. G. 2000 Large eddy simulation of naturally induced fire whirls in a vertical square channel with corner gaps. *ASME Heat Transfer Div Publ HTD* **366**, 73–80.

GRAHAM, H. E. 1952 A fire-whirlwind of tornadic violence. *Fire Control Notes* **13**, 22–24.

GRAHAM, H. E. 1957 Fire whirlwind formation as favored by topography and upper winds. *Fire Control Notes* **18**, 20–24.

MCGRATTAN, K. B. 2004 Fire dynamics simulator (version 4) c technical reference guide. *Tech. Rep.* 1018. National Institute of Standards and Technology, special Publication.

MERONEY, R. N. 2003*a* Fire whirls and building aerodynamics. In *Proc. 11th Int. Conf. on Wind Engineering*.

MERONEY, R. N. 2003*b* Fire whirls, fire tornadoes, and fire storms: Physical and numerical modeling. In *Proc. PHYSMOD'03: Intl. Workshop on Physical Modelling of Flow and Dispersion Phenomena*.

MERONEY, R. N. 2004 Fires in porous media: Natural and urban canopies. In *NATO Advanced Study Institute on Flow and Transport Processes in Complex Obstructed Geometries: From Cities and Vegetative Canopies to Industrial Problems*. ASME.

RYDER, N. L., SCHEMEL, C. F. & JANKIEWICZ, S. P. 2006 Near and far field contamination modeling in a large scale enclosure: Fire dynamics simulator comparisons with measured observations. *J. Hazard. Mater.* **130**, 182–186.

Ryder, N. L., Sutula, J. A., C. F., Schemel, Hamer, A. J. & Van Brunt, V. 2004 Consequence modeling using the fire dynamics simulator. *J. Hazard. Mater.* **115**, 149–154.

Satoh, K. & Yang, K. T. 1996 Experimental observations of swirling fires. In *Proc. 1996 ASME Intl. Mechanical Engineering Congress and Exposition. Part 1*, pp. 393–400. ASME.

Satoh, K., Zhu, J. P., Liu, N. & Yang, K. T. 2005 Experiments and analysis of interaction among multiple fires in equidistant fire arrays. In *Proc. ASME Summer Heat Transfer Conf.* Elsevier (in press).

Yi, L., Chow, W. K., Li, Y. Z. & Huo, R. 2005 A simple two-layer zone model on mechanical exhaust in an atrium. *Building Environ.* **40**, 869–880.